Effect of wall perturbations on the receptivity of a hypersonic boundary layer

Xiaowen Wang[a] and Xiaolin Zhong
Department of Mechanical and Aerospace Engineering, University of California at Los Angeles, Los Angeles, California 90095, USA

(Received 14 February 2008; accepted 17 December 2008; published online 8 April 2009)

The receptivity of a Mach 5.92 flat plate boundary layer to periodic two-dimensional wall perturbations is studied by numerical simulations and linear stability theory (LST). Free stream flow conditions are the same as the leading edge receptivity experiment of Maslov *et al.*, J. Fluid Mech. **426**, 73 (2001). Steady base flow is simulated by solving compressible Navier–Stokes equations with a combination of a fifth-order shock-fitting method and a second-order total variation diminishing scheme. The accuracy of the steady base flow is validated by comparisons with the experimental measurements of Maslov *et al.* and self-similar boundary-layer solution. In receptivity simulations, streamwise velocity perturbation, blowing suction, and temperature perturbation are introduced to the steady base flow with a forcing slot on flat plate. A model of wall perturbation is proposed based on physical properties of the electric pulse generator used in the experiment of Maslov *et al.* Stability characteristics of boundary-layer waves are identified and evaluated by comparing the results of LST and numerical simulation. Numerical simulation results show that all three types of wall perturbations eventually result in the same type of instability wave (mode *S*) in the boundary layer, which indicates that receptivity mechanism of the hypersonic boundary layer to wall perturbation is independent of specific perturbation type. On the other hand, the hypersonic boundary layer is found to be most sensitive to blowing-suction and least sensitive to temperature perturbation. © *2009 American Institute of Physics*. [DOI: 10.1063/1.3103880]

I. INTRODUCTION

Due to the fact that a turbulent boundary layer generates much higher shear stress and heat flux than a laminar one, laminar-turbulent transition significantly affects aerodynamic performance and thermal protection system of hypersonic transportation vehicles and re-entry vehicles. Therefore, accurate prediction of boundary-layer transition is very important to drag calculation and aerothermal design of hypersonic vehicles.

In order to predict and control boundary-layer transition, extensive studies have been carried out to reveal transition mechanisms.[1–5] It is recognized that the process of boundary-layer transition strongly depends on the amplitude level of environmental perturbations.[6–8] In an environment of small amplitude perturbations, transition over a smooth surface is mainly caused by the instability of boundary-layer wave. The corresponding transition generally consists of the following three stages:

- Stage 1: receptivity process during which small amplitude environmental perturbations enter the boundary layer and excite boundary-layer waves;
- Stage 2: linear development or growth of unstable boundary-layer waves which can be predicted by solving the eigenproblem of homogeneous linearized stability equations;
- Stage 3: boundary-layer transition caused by nonlinear growth and three-dimensional effects when the unstable waves reach certain amplitudes.

To high amplitude perturbations, laminar boundary-layer flow can breakdown to turbulence right after the receptivity process due to strong initial excitations of boundary-layer waves. On the other hand, for boundary-layer flows over nonsmooth surface, strong transient growth induced by surface roughness may directly lead to transition.[6–8] All these transition mechanisms related to high amplitude perturbations and transient growth are called bypass transition.

Receptivity process is of critical importance to transition prediction because it provides initial conditions of amplitude, frequency, and phase angle for boundary-layer waves.[9] Although low-speed receptivity has been relatively well understood,[8,10] receptivity process of supersonic and hypersonic boundary-layer flows is more complex than that of low-speed flows due to additional effects of compressibility, shock wave, high temperature, etc. Recently, theoretical, experimental, and numerical simulation studies on the excitations of boundary-layer waves in two- and three-dimensional supersonic and hypersonic boundary layers have been carried out by many researchers.[4,11–15]

Mack[1] was the first to carry out extensive computations on linear stability characteristics of the compressible boundary layer. He used compressible linear stability theory (LST) to calculate the amplitude ratio (A/A_0) of constant-frequency disturbances as a function of Reynolds number, where A and A_0 were local disturbance amplitude and initial disturbance

[a]Electronic mail: xiaowen@seas.ucla.edu.

amplitude. The transition Reynolds number was determined by an amplitude-ratio criterion. For a cooled-wall flat plate supersonic boundary layer, it was found that the calculated transition Reynolds number increased much faster than that measured in his experiments. Such results indicated that LST alone was insufficient to accurately determine transition Reynolds number. It was necessary to consider the properties of environmental disturbances and initial excitations of boundary-layer waves. Fedorov[15] investigated the mechanisms of instability wave excitation in flat plate boundary layers by temperature perturbation and blowing-suction located on the body surface. It was found that blowing-suction was more effective in generating instability waves. Hanifi *et al.*[16] studied the temporal transient growth phenomena of boundary-layer flows at a series of Mach numbers from 0.1 to 4.5 using spectral collocation method. They found that the maximum transient growth increased with Mach number increasing, and it could be scaled with R^2, square of the Reynolds number based on the local length scale of boundary-layer thickness. In addition, the time at which the maximum transient growth was reached could be scaled with R. Fedorov and Khokhlov[11] studied the receptivity of hypersonic boundary layers over a flat plate to wall disturbances with a combination of asymptotic method and numerical simulation. They found that strong excitations occurred in local regions where forcing disturbances were resonant with boundary-layer waves. When the resonance point of forcing and boundary-layer wave approached the lower neutral point of the second mode, near the synchronization point of the first mode and the second mode, the receptivity coefficient tended to infinity. By using asymptotic method, this singularity was successfully resolved and the receptivity coefficient was found to be extremely high. They also found that hypersonic boundary layers were more sensitive to blowing-suction disturbances than to wall vibrations and temperature disturbances. Forgoston and Tumin[17] studied the three-dimensional wave packet generated by a local temperature spot in a hypersonic boundary layer. They showed that the solution to this initial-value problem could be expanded in a biorthogonal eigenfunction system as a sum of discrete and continuous modes. The inverse Fourier transforms for modes F and S were computed and agreed well with the corresponding asymptotic approximations of the Fourier integral. Recently, Tumin[18] calculated three-dimensional spatially growing perturbations in a two-dimensional compressible boundary layer. Within the scope of linearized Navier–Stokes equations, the solution could be presented as an expansion into a biorthogonal eigenfunction system.

Due to the difficulties in carrying out supersonic and hypersonic receptivity experiments, very few experimental studies have been reported. Kendall[2] experimentally studied the growth of natural fluctuations in zero pressure gradient boundary layers at several Mach numbers ranging from 1.6 to 8.5. Substantial growths of flow fluctuations were observed within the laminar boundary layer in the early region where the boundary layer was predicted to be linearly stable. The growth rates of these fluctuations in the region downstream of the initial growth were in a reasonable agreement with the LST results of Mack.[1] Kosinov and Maslov[19] investigated the growth of artificially induced disturbances in a supersonic boundary layer. The disturbances were measured by a hot-wire anemometer. Fourier components of experimentally measured disturbances were calculated and compared to the theoretical results of LST in a parallel flow approximation. Their results showed a qualitative match between experimental and theoretical disturbance growths. Maslov and Semenov[20] studied the receptivity of a supersonic boundary layer to artificial acoustic waves by utilizing two parallel flat plates. The acoustic waves generated by an electric discharge system on the lower plate radiated into the external flow and penetrated into the boundary layer of the upper plate as free stream acoustic disturbances. It was found that the acoustic disturbances were converted into boundary-layer waves most efficiently at the leading edge, in the neighborhood of lower and upper branches of the neutral curve. A similar experiment was carried out on a Mach 5.92 boundary-layer flow by Maslov *et al.*[4] to study leading edge receptivity. It was observed that Tollmien–Schlichting waves were generated by acoustic waves impinging on the leading edge. They also found that receptivity coefficients strongly depended on wave inclination angles. Kosinov *et al.*[21] investigated the excitation of unstable boundary-layer waves at the leading edge of a flat plate. In their experiments, controlled external disturbances were generated by an electric discharge system on the lower plate then impinged on the leading edge of the upper flat plate. In order to figure out generation coefficients, amplitudes of disturbances near the leading edge and the excited waves inside the boundary layer were measured by a constant-temperature hot-wire anemometer and a single-wire probe. They found that both Tollmien–Schlichting waves and acoustic waves were generated in the boundary layer.

Recently there have been many numerical simulation studies in supersonic and hypersonic boundary-layer receptivity. Collis and Lele[22] numerically investigated the formation of stationary cross-flow vortices in a three-dimensional boundary layer due to surface roughness located near the leading edge of a swept wing. The results showed that convex surface curvature enhanced receptivity while nonparallel effects strongly reduced initial amplitude of stationary cross-flow vortices. Malik *et al.*[3] investigated the responses of a Mach 8 flow over a sharp wedge of a half angle of 5.3° to three types of external forcing: a planar free stream acoustic wave, a narrow acoustic beam enforced on the bow shock near the leading edge, and a blowing-suction slot on the wedge surface. They concluded that these three types of forcing eventually resulted in the same type of instability waves in the boundary layer. Zhong[23] studied acoustic receptivity of a hypersonic flow over a parabola by solving full Navier–Stokes equations. It was found that generations of boundary-layer waves were mainly caused by the interaction of the boundary layer with the transmitted acoustic waves instead of entropy and vorticity waves. In a series of papers, Ma and Zhong[5,13,14] studied the receptivity of a supersonic boundary layer to various free stream disturbances with a combination of numerical simulation and LST. It was found that, in addition to conventional first and second Mack waves, there existed a family of stable waves which played an important

role in the excitation of unstable waves. Egorov *et al.*[24] numerically solved unsteady two-dimensional flows relevant to the receptivity of supersonic and hypersonic boundary layers using a total variation diminishing (TVD) scheme. To compare with numerical simulation results, theoretical analysis was carried out with parallel LST and nonparallel LST. It was noticed that nonparallel effect stabilized the second mode. For small forcing amplitudes, the second mode growth rates obtained from numerical simulation had a good agreement with those predicted by nonparallel LST. Their simulations also showed nonlinear saturation of fundamental harmonic and rapid growth of higher harmonics. Wang[25] studied the receptivity of the same hypersonic boundary layer as in the investigation of Malik *et al.*[3] to periodic blowing-suction disturbances introduced in a narrow region on the wall. The effects of frequency, location, and length of the blowing-suction slot on receptivity were investigated based on series of numerical simulations. The numerical results showed that mode *F*, mode *S*, and acoustic modes were excited by wall blowing suction. Far downstream of the forcing region, mode *S* became the dominant mode in the boundary layer. All cases of numerical simulations consistently showed that the synchronization point of modes *F* and *S* played an important role in the excitation of mode *S*. Mode *S* was strongly excited when the blowing-suction slot was located upstream of the synchronization point. On the other hand, when the blowing-suction slot was downstream of the synchronization point, there was a very weak excitation of mode *S*, despite the fact that the blowing-suction slot was still within the unstable region of mode *S*. A concurrent theoretical study was carried out by Tumin *et al.*[12] to compare theoretical and numerical results of receptivity coefficients and to analyze receptivity characteristics. The perturbation field downstream of the blowing-suction slot was decomposed into boundary-layer waves with the help of a biorthogonal eigenfunction system. It was found that there was a good agreement between normal-mode amplitudes calculated with the help of the theoretical receptivity model and those obtained from projecting the numerical results onto the normal modes. Egorov *et al.*[26] studied stability and receptivity of a Mach 6 flow over a flat plate with a porous coating by numerically solving two-dimensional Navier–Stokes equations. Their numerical results were in a good agreement with theoretical analysis based on LST. It was confirmed that the porous coating stabilized the supersonic boundary layer. Zhong and Ma[27] numerically studied the receptivity of a Mach 7.99 axisymmetric flow over a 7° half-angle blunt cone to free stream fast acoustic waves. They found that no Mack modes were excited by free stream fast acoustic waves in early region along the cone surface. The delay of the second mode excitation was owing to the fact that the hypersonic boundary-layer receptivity was governed by a two-step resonant interaction process.

In this paper, the receptivity of a Mach 5.92 flat plate boundary layer to periodic two-dimensional wall perturbations is studied by numerical simulations and LST. The objectives of the current research are to study the receptivity of the hypersonic boundary layer to wall perturbations, and to investigate the effect of different wall perturbation on receptivity. Free stream flow conditions of the hypersonic boundary layer are the same as those of the leading edge receptivity experiment of Maslov *et al.*[4] Steady base flow is simulated first by solving two-dimensional compressible Navier–Stokes equations with a combination of a fifth-order shock-fitting finite difference method and a second-order TVD scheme. The accuracy of the steady base flow is validated by comparisons with the experimental measurements of Maslov *et al.* and self-similar boundary-layer solution. In receptivity simulations, periodic wall perturbations are introduced to the steady base flow at a forcing slot located on the flat plate. A model of wall perturbation is proposed based on physical properties of the electric pulse generator used in the experiment of Maslov *et al.* Stability characteristics of boundary-layer waves are identified and evaluated by comparing the results of LST and numerical simulations. The effect of wall perturbation on the receptivity is investigated by considering three types of perturbations: streamwise velocity perturbation, blowing-suction, and temperature perturbation.

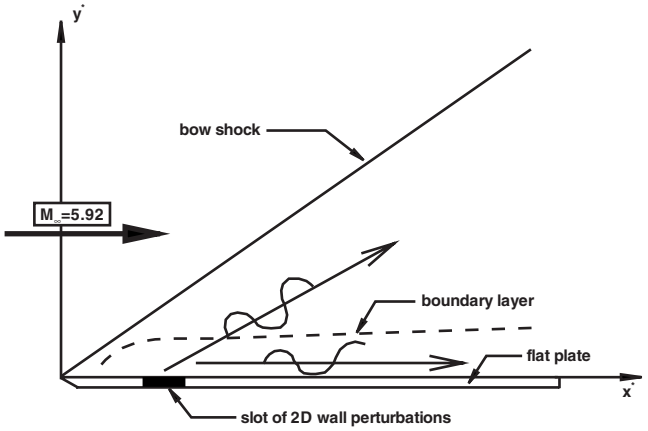

FIG. 1. A schematic of the receptivity of a Mach 5.92 flow over a flat plate to periodic two-dimensional wall perturbations.

II. GOVERNING EQUATIONS AND NUMERICAL METHODS

In current numerical studies, a Mach 5.92 boundary layer over a flat plate as shown in Fig. 1 is considered. The flow is assumed to be thermally and calorically perfect. Governing equations of numerical simulations are compressible Navier–Stokes equations in the conservative form, i.e.,

$$\frac{\partial \vec{U}^*}{\partial t^*} + \frac{\partial}{\partial x_1^*}(\vec{F}_{1i}^* + \vec{F}_{1v}^*) + \frac{\partial}{\partial x_2^*}(\vec{F}_{2i}^* + \vec{F}_{2v}^*) = 0, \tag{1}$$

where $\vec{U}^*$ is a column vector containing conservative variables of mass, momentum, and energy, i.e.,

$$\vec{U}^* = \{\rho^*, \rho^* u_1^*, \rho^* u_2^*, e^*\}^T. \tag{2}$$

In this paper, the superscript "*" represents dimensional variables. Flux vectors in Eq. (1) are divided into their inviscid and viscous components because the two components are discretized with different schemes. The components, $\vec{F}_{1i}^*$ and

$\vec{F}^*_{2i}$, stand for inviscid flux whereas $\vec{F}^*_{1v}$ and $\vec{F}^*_{2v}$ are viscous flux components. The flux components are written as

$$\vec{F}^*_{ji} = \begin{bmatrix} \rho^* u^*_j \\ \rho^* u^*_1 u^*_j + p^* \delta_{1j} \\ \rho^* u^*_2 u^*_j + p^* \delta_{2j} \\ u^*_j (e^* + p^*) \end{bmatrix},$$

$$\vec{F}^*_{jv} = \begin{bmatrix} 0 \\ -\tau^*_{1j} \\ -\tau^*_{2j} \\ -\tau^*_{1j} u^*_1 - \tau^*_{2j} u^*_2 + k^* \dfrac{\partial T^*}{\partial x^*_j} \end{bmatrix}, \tag{3}$$

with $j \in \{1,2\}$. In Eq. (3), δ_{ij} $(i=1,2)$ is the Kronecker Delta function. In perfect gas assumption, pressure and energy are given by

$$p^* = \rho^* R^* T^*, \tag{4}$$

$$e^* = \rho^* c^*_v T^* + \frac{\rho^*}{2}(u^{*2}_1 + u^{*2}_2), \tag{5}$$

where R^* is gas constant, and c^*_v is specific heat at constant volume. For compressible Newtonian flow, the viscous stress tensor is calculated as follows:

$$\tau^*_{ij} = \mu^* \left(\frac{\partial u^*_i}{\partial x^*_j} + \frac{\partial u^*_j}{\partial x^*_i} \right) - \frac{2}{3} \mu^* \left(\frac{\partial u^*_1}{\partial x^*_1} + \frac{\partial u^*_2}{\partial x^*_2} \right) \delta_{ij}, \tag{6}$$

with $i,j \in \{1,2\}$. In current simulation, viscosity coefficient, μ^*, and heat conductivity coefficient, k^*, are calculated using Sutherland's law together with a constant Prandtl number, Pr. They are both functions of temperature only,

$$\mu^* = \mu^*_r \left(\frac{T^*}{T^*_r} \right)^{3/2} \frac{T^*_r + T^*_s}{T^* + T^*_s}, \tag{7}$$

$$k^* = \frac{\mu^* c^*_p}{Pr}, \tag{8}$$

where $\mu^*_r = 1.7894 \times 10^{-5}$ N s/m^2, $T^*_r = 288.0$ K, $T^*_s = 110.33$ K, and c^*_p is specific heat at constant pressure.

Dimensional flow variables are nondimensionalized by free stream parameters. Specifically, density, temperature, velocity, and pressure are scaled by ρ^*_∞, T^*_∞, u^*_∞, and $\rho^*_\infty u^{*2}_\infty$. Furthermore, x^*_1 is nondimensionalized by unit length in meters, whereas x^*_2 is nondimensionalized by the local length scale of boundary-layer thickness, $\sqrt{\mu^*_\infty x^*_1 / \rho^*_\infty u^*_\infty}$. Referring to the coordinate system shown in Fig. 1, x^*_1 and x^*_2 are x^* and y^*, respectively. The two variables, u^*_1 and u^*_2, are velocities in streamwise and wall-normal directions. In order to show numerical simulation results clearly and make it easy to compare flow field between numerical simulation and the experimental measurement of Maslov *et al.* both dimensional and nondimensional variables are used in current paper to plot results.

The fifth-order shock-fitting finite difference method of Zhong[28] is used to solve the governing equations in a domain bounded by bow shock and flat plate. In other words, bow shock is treated as a boundary of the computational domain. Rankine–Hugoniot relations across the shock and a characteristic compatibility relation coming from downstream flow are combined to solve flow variables behind the shock. The shock-fitting method makes it possible for Navier–Stokes equations to be spatially discretized by high-order finite difference methods. Specifically, a fifth-order upwind scheme is applied to discretize inviscid flux derivatives. Meanwhile, a sixth-order central scheme is used for the discretization of viscous flux derivatives. By using shock-fitting method, the interaction between bow shock and wall forcing induced perturbations is solved as a part of solutions with position and velocity of the shock being solved as dependent flow variables. Runge–Kutta methods are used for temporal integration. In leading edge region, there exists a singular point at the tip of the flat plate, which will introduce numerical instability if the fifth-order shock-fitting method is used to simulate flow. Therefore, the computational domain for shock-fitting simulation starts from a very short distance downstream of the leading edge. A second-order TVD scheme used by Zhong and Lee[29] is applied to simulate steady base flow in a small region including the leading edge to supply inlet conditions for shock-fitting simulation. In receptivity simulations, two-dimensional wall perturbations are introduced in a downstream region so that the fifth-order shock-fitting method can be used to simulate the responses of the boundary layer to external perturbations.

The same numerical method has been used by Ma and Zhong[5,13,14] in their receptivity studies of supersonic and hypersonic boundary layers over a flat plate and a sharp wedge to various free stream disturbances. The good agreement between numerical and LST results indicates that the fifth-order shock-fitting finite difference method is accurate to simulate receptivity problems of high-speed boundary-layer flows. The numerical method has also been validated in a theoretical study and comparison with numerical simulation of Tumin *et al.*,[12] where numerical perturbation field downstream of the blowing-suction slot was decomposed into boundary-layer waves with the help of a biorthogonal eigenfunction system. The results showed a good agreement between normal-mode amplitudes calculated with a theoretical receptivity model and those obtained from projecting numerical results onto normal modes.

III. FLOW CONDITIONS AND PERTURBATION MODEL

Free stream flow conditions of the hypersonic boundary-layer flow are the same as the experiment of Maslov *et al.*,[4] i.e.,

$$M_\infty = 5.92, \quad T^*_\infty = 48.69 \text{ K},$$

$$p^*_\infty = 742.76 \text{ Pa}, \quad \text{Pr} = 0.72,$$

$$f^* = 50 \text{ kHz}, \quad F = 3.0 \times 10^{-5},$$

$$\text{Re}^*_\infty = 13 \times 10^6/\text{m}, \quad \gamma = 1.4,$$

where Re^*_∞ is unit Reynolds number defined as

$$\mathrm{Re}_\infty^* = \rho_\infty^* u_\infty^* / \mu_\infty^*. \tag{9}$$

In free stream, Sutherlands law is not valid for such low temperature as $T_\infty^*=48.69$ K. However, numerical simulations are carried out for flow after the shock, where temperature is much higher than free stream temperature. Therefore, it is valid to use Sutherlands law in our numerical simulations.

The streamwise coordinate, x^* as shown in Fig. 1, can be converted to local Reynolds number by

$$\mathrm{Re}_x = \mathrm{Re}_\infty^* x^*. \tag{10}$$

In LST analysis, Reynolds number based on the local length scale of boundary-layer thickness, L^*, is generally used. They are expressed as

$$R = \frac{\rho_\infty^* u_\infty^* L^*}{\mu_\infty^*}, \quad L^* = \sqrt{\frac{\mu_\infty^* x^*}{\rho_\infty^* u_\infty^*}}. \tag{11}$$

Hence, the relation between R and local Reynolds number Re_x is given by

$$R = \sqrt{\mathrm{Re}_x}. \tag{12}$$

In both steady and unsteady simulations, inlet conditions are specified. High-order extrapolation is used for outlet conditions because the flow is hypersonic at the exit except a small region near the flat plate. Flow variables behind the shock are solved by combining Rankine–Hugoniot relations across the shock and a characteristic compatibility relation coming from downstream flow.

For steady base flow simulation, the wall is adiabatic, and the physical boundary condition of velocity on flat plate is nonslip condition. In receptivity simulations, special treatment of wall boundary conditions is needed. When streamwise velocity perturbation and blowing suction are introduced, temperature perturbation is set to zero, which is a standard boundary condition for theoretical and numerical studies of high frequency disturbances. Meanwhile, nonslip condition is applied on flat plate except the forcing region. On the other hand, when temperature perturbation is introduced, temperature perturbation is set to zero except the forcing region. Meanwhile, nonslip condition is applied on flat plate.

In the experiments of Maslov *et al.*,[4] leading edge receptivity of a Mach 5.92 flow over a flat plate to two- and three-dimensional artificial disturbances was investigated. An electric pulse generator centered at $x^*=35$ mm ($R=2133.07$) was used to introduce disturbances. It generated high-voltage electric pulses with a duration of 2 μs and at a frequency of 50 kHz. Experimental results showed that disturbances were introduced by a local glow discharge when voltages on electrodes were comparably low (600 V). When voltages on electrodes were increased to 700 V, size of the glow discharge increased and a flat streamwise extended oval was also observed. Maslov *et al.* analyzed physical properties of the forcing disturbances and found that the glow discharge introduced disturbances through a blowing-suction mechanism whereas the streamwise extended oval introduced thermal energy. In addition, the air between electrodes was partially ionized when high voltages are imposed. Ions moved toward electrodes due to Coulomb force, which lead to streamwise velocity perturbation near the wall.

Based on physical properties of the electric pulse generator used in the experiments of Maslov *et al.*, a model of periodic two-dimensional wall perturbation is proposed in this paper, which consists of streamwise velocity perturbation, blowing suction, and temperature perturbation. The model is mathematically expressed as

$$\begin{pmatrix} u^{*\prime} \\ (\rho v)^{*\prime} \\ T^{*\prime} \end{pmatrix} = \begin{pmatrix} Q_u \epsilon_1 F(l_1)(du^*/dy^*)_{y^*=0} \\ Q_v \epsilon_2 G(l_2)(\rho u)_\infty^* \\ Q_T \epsilon_3 H(l_3) T_\infty^* \end{pmatrix} S(t^*), \tag{13}$$

where the superscript " $'$ " represents disturbance. $(du^*/dy^*)_{y^*=0}$ is the derivative of streamwise velocity on flat plate calculated from numerical steady base flow, whereas $(\rho u)_\infty^*$ and T_∞^* are streamwise mass flux and temperature in free stream, respectively. In Eq. (13), Q_u, Q_v, and Q_T are three constants with the value being either 1 or 0. A combination of (Q_u, Q_v, Q_T) determines perturbation type. For example, (1, 0, 0) is the case of streamwise velocity perturbation, (0, 1, 0) is the case of blowing suction, whereas (0, 0, 1) is the case of temperature perturbation. The three parameters, ϵ_1, ϵ_2, and ϵ_3, represent dimensionless amplitudes of perturbations. In receptivity simulations, dimensionless amplitudes are small enough to preserve linear properties of perturbations. $F(l_1)$, $G(l_2)$, and $H(l_3)$ are perturbation profile functions. The three variables, l_1, l_2, and l_3, are dimensionless coordinates defined within forcing region $(x_i^* \le x^* \le x_e^*)$, where x_i^* and x_e^* are coordinates of the leading and trailing edges of the forcing slot. In the experiments of Maslov *et al.*, x_i^* and x_e^* are equal to 33 and 37 mm ($R=654.98$ and 693.54), respectively. In Eq. (13), $S(t^*)$ is a function of time defined as

$$S(t^*) = \begin{cases} 1, & \text{if } \mathrm{mod}(t^*, 20\ \mu\mathrm{s}) \le 2\ \mu\mathrm{s} \\ 0, & \text{if } \mathrm{mod}(t^*, 20\ \mu\mathrm{s}) > 2\ \mu\mathrm{s}, \end{cases} \tag{14}$$

where mod is the residual function. The value 20 μs is the period of perturbation at a frequency of $f^*=50$ kHz. Whereas the value 2 μs is the time interval during which perturbation is enforced, because the electric pulse used in the experiments of Maslov *et al.* only has a duration of 2 μs.

Due to linear properties of perturbations, the temporal function $S(t^*)$ can be decomposed to its sinusoidal components using Fourier cosine transform, i.e.,

$$S(t^*) = \sum_{n=0}^{\infty} b_n \cos(2\pi n f^* \tau^*), \tag{15}$$

where $\tau^*=t^*-1$ μs. The coefficients b_n are calculated as

$$b_n = \begin{cases} 0.1, & \text{if } n=0 \\ \dfrac{2\sin\left(\dfrac{n\pi}{10}\right)}{n\pi}, & \text{if } n=1,2,3,\ldots. \end{cases} \tag{16}$$

Figure 2 shows the coefficients b_n of sinusoidal components. It is noticed that sinusoidal component at the frequency of $f^*=50$ kHz ($n=1$) has the maximum amplitude. When the

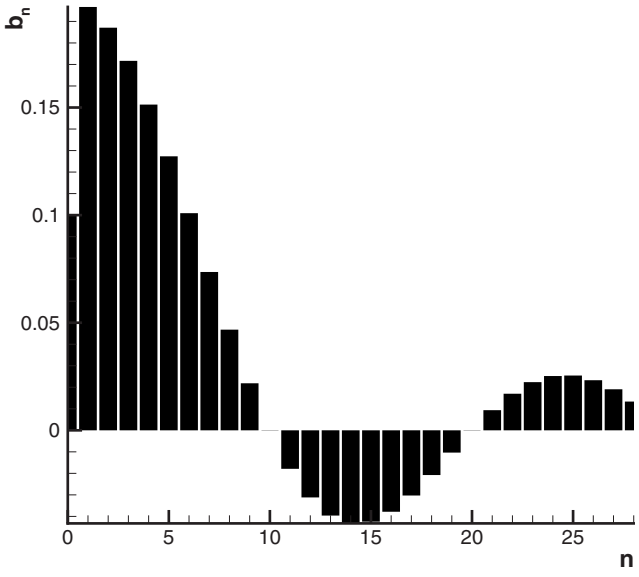

FIG. 2. The coefficients b_n of sinusoidal components.

coefficient b_n is negative, the corresponding sinusoidal component has a 180° phase angle discrepancy to the first sinusoidal component.

Dimensional circular frequency of wall perturbations is related to dimensional frequency by

$$\omega^* = 2\pi f^*. \tag{17}$$

Dimensional circular frequency and frequency are nondimensionalized as follows:

$$\omega = \frac{\omega^* L^*}{u_\infty^*}, \tag{18}$$

$$F = \frac{2\pi f^* \mu_\infty^*}{\rho_\infty^* u_\infty^{*2}} = \frac{\omega^* \mu_\infty^*}{\rho_\infty^* u_\infty^{*2}}. \tag{19}$$

With the definitions of Reynolds number R and dimensionless frequency F, dimensionless circular frequency can also be expressed as

$$\omega = RF. \tag{20}$$

IV. STEADY BASE FLOW

Steady base flow is simulated by solving two-dimensional compressible Navier–Stokes equations with a combination of a fifth-order shock-fitting finite difference method and a second-order TVD scheme. In leading edge region, there exists a singular point at the tip of flat plate, which will introduce numerical instability if the fifth-order shock-fitting method is used. Therefore, a second-order TVD scheme used by Zhong and Lee[29] is applied to simulate steady base flow in a small region including the leading edge. Computational domain for the fifth-order shock-fitting method starts at $x^*=0.0025$ m and ends at $x^*=0.879$ m, corresponding to $R=180.28$ and $R=3380.38$, respectively. In actual simulations, the computational domain is divided into 19 zones with a total of 3746 grid points in streamwise direction. The number of grid points in wall-normal direction is 121 upstream of $x^*=0.309$ m ($R=2004.24$) and 176 downstream of that position. 41 points are used in the overlapped region between two neighboring zones, which is proved to be sufficient to make the solution accurate and smooth within the whole domain. An exponential stretching function is used in wall-normal direction to cluster more points inside the boundary layer. On the other hand, the grid points are uniformly distributed in streamwise direction. Spatial convergence of the results based on this grid structure has been evaluated by grid refinement studies.

For shock-fitting simulation in the first zone, inlet conditions are obtained from the results of shock-capturing simulation in a small region including the leading edge, where a second-order TVD scheme is used to simulate steady base flow. For shock-fitting simulations in other zones, inlet conditions are interpolated from the results of previous zone. Computational domain for shock-capturing simulation starts at $x^*=-0.0005$ m and ends at $x^*=0.0035$ m ($R=213.31$). Three sets of grid structures are used to check grid independence of numerical simulation results. Figure 3(a) compares density contours near the leading edge for three sets of grid structures. It shows that density contours on 201×176 mesh agree well with those on 241×181 mesh, whereas they have significant discrepancies with density contours on 161×101 mesh. This figure indicates that the grid structure of 201×176 is fine enough to ensure grid independence of numerical simulation results. However, the grid structure of 161×101 is too coarse to achieve spatially converged results. Similar conclusion can be drawn in Fig. 3(b), where density distributions in wall-normal direction are compared. In this figure, density distributions are evaluated at $x^*=0.0025$ m ($R=180.28$).

To validate the combination of the fifth-order shock-fitting method and the second-order TVD scheme, Figs. 4(a) and 4(b), compares wall-normal velocity contours and distributions near the leading edge obtained by the combination of a second-order TVD scheme and a fifth-order shock-fitting method. Flow field including the leading edge is simulated by TVD scheme, while flow field after $x^*=0.0025$ m ($R=180.28$) is simulated by shock-fitting method. Figure 4(a) shows that wall-normal velocity contours calculated by the two methods have a good agreement near the upstream edge of the overlapped region, which indicates that TVD solutions are accurate enough to be used as inlet conditions for the fifth-order shock-fitting simulation in the first zone. The small discrepancies of the contours near bow shock are caused by viscous effect. Due to viscosity, bow shock has a finite thickness for TVD simulation, while it is assumed to be infinitely thin for shock-fitting simulation. Similar conclusion can be drawn in Fig. 4(b), where wall-normal velocity distributions at the location of $x^*=0.003$ m ($R=197.4$) are compared. The combination of a fifth-order shock-fitting method and a second-order TVD scheme has also been validated in cases of supersonic and hypersonic steady base flows by Ma and Zhong[5,13,14] and Wang.[25]

Figures 5(a) and 5(b) shows pressure contours of steady base flow computed by the fifth-order shock-fitting method. In Fig. 5(a), the upper boundary of flow field represents bow shock induced by displacement thickness of the boundary

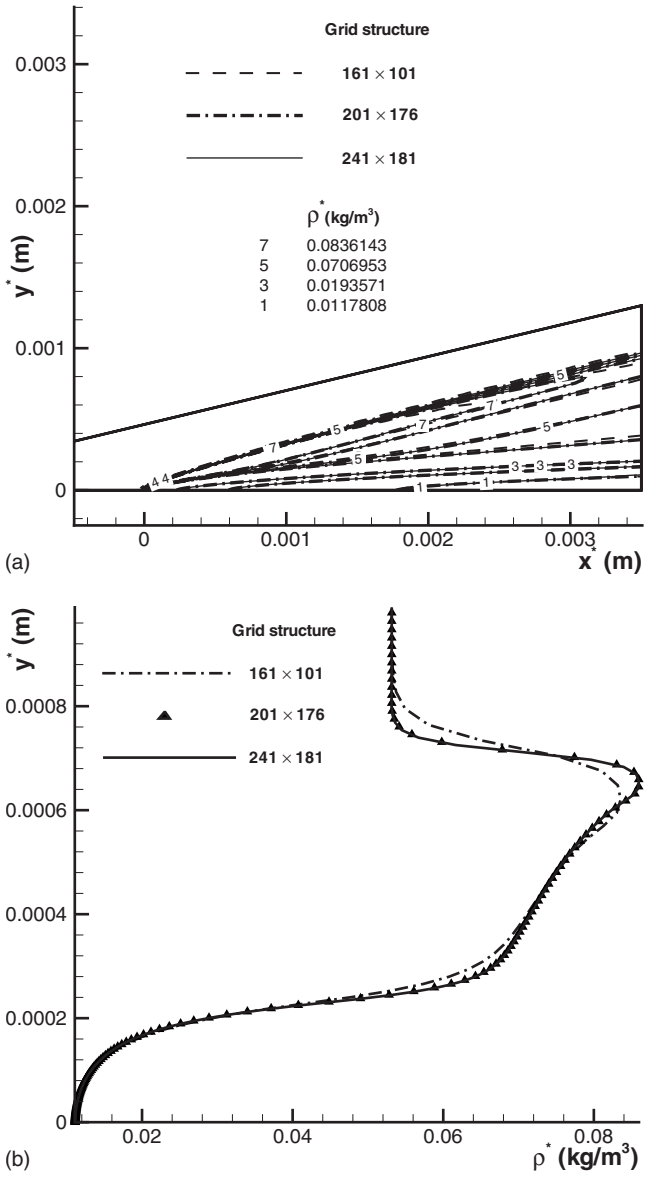

FIG. 3. Comparisons of density contours and wall-normal distributions for three sets of grid structures.

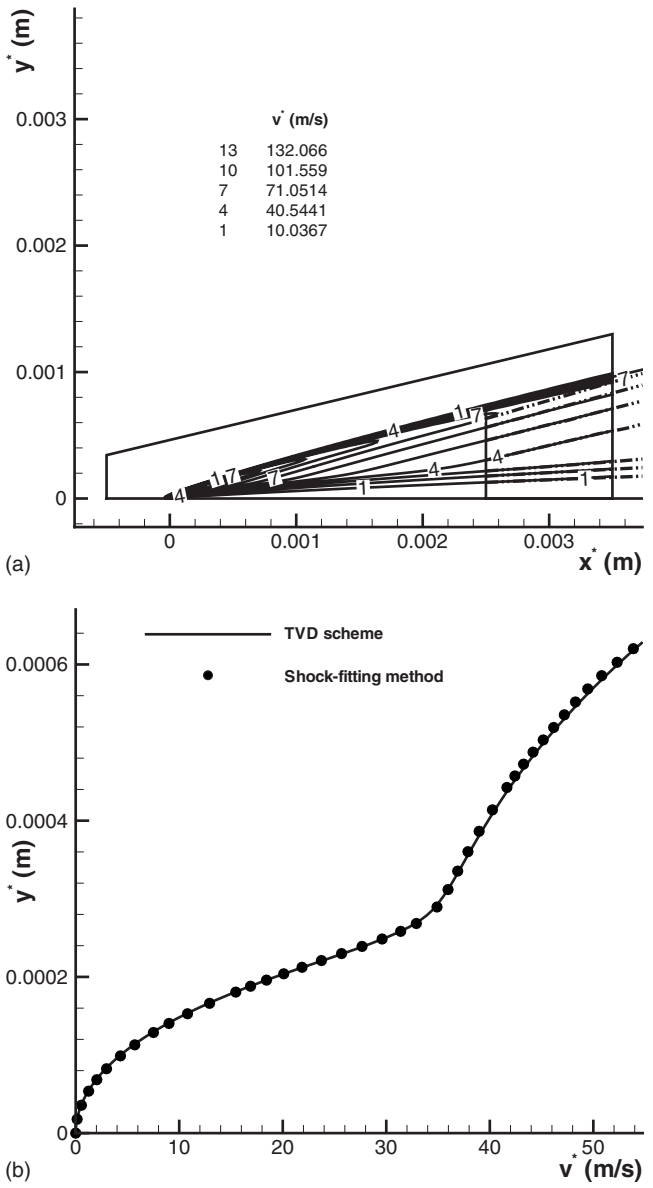

FIG. 4. Comparisons of wall-normal velocity contours and distributions near the leading edge.

layer. The lower boundary is the flat plate. A part of pressure contours from $x^*=0.33$ m to $x^*=0.36$ m ($R=2071.23$ to $R=2163.33$) is amplified in Fig. 5(b) to show clearly pressure distributions within the boundary layer. It is noticed that pressure is approximately a constant across the boundary layer and along the Mach lines, which is consistent with boundary layer theory and inviscid supersonic aerodynamics. At a fixed location (constant x^*), pressure behind the shock is higher than that on flat plate due to the existence of bow shock. Figure 6 shows distributions of wall pressure and pressure behind bow shock computed by the fifth-order shock-fitting method. Large pressure gradient near the leading edge is caused by the interaction between viscous boundary layer and inviscid outer flow. From upstream to downstream, viscous-inviscid interaction becomes weaker with bow shock moving away from the boundary layer. As a result, pressure approaches a constant further downstream with pressure gradient decreasing. Again, Fig. 6 shows that at a fixed location (constant x^*), pressure behind the shock is higher than that on flat plate.

Figure 7 shows bow shock position and distribution of Mach number behind the shock. In this figure, a straight line tangential to shock near the leading edge is plotted helping to illustrate that the shock is not a straight line. A decrease in shock angle from upstream to downstream indicates that the shock becomes weaker downstream. The dramatic increase of Mach number near the leading edge is also due to interaction between viscous boundary layer and inviscid outer flow. After $x^*=33$ mm ($R=654.98$), intensity of viscous-inviscid interaction decreases quickly with blow shock moving away from the boundary layer. Mach number behind the shock approaches a constant downstream. The increase in Mach number also indicates that bow shock becomes weaker from upstream to downstream.

In order to check the accuracy of numerical simulation, steady base flow simulated by the fifth-order shock-fitting

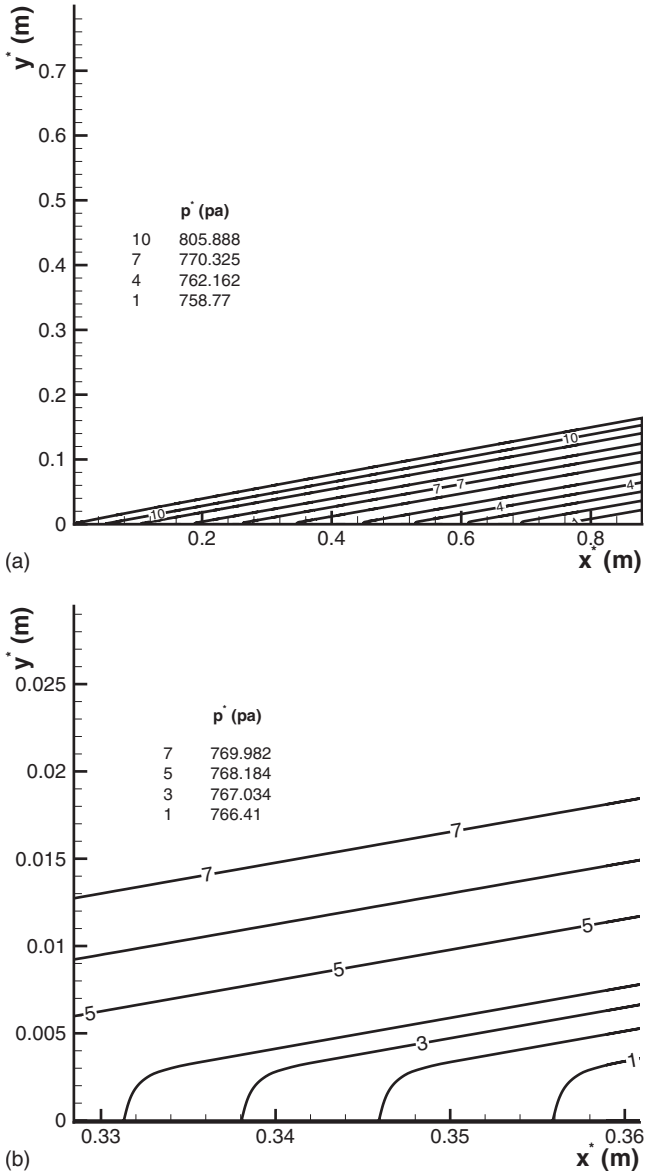

FIG. 5. Pressure contours of steady base flow computed by the fifth-order shock-fitting method.

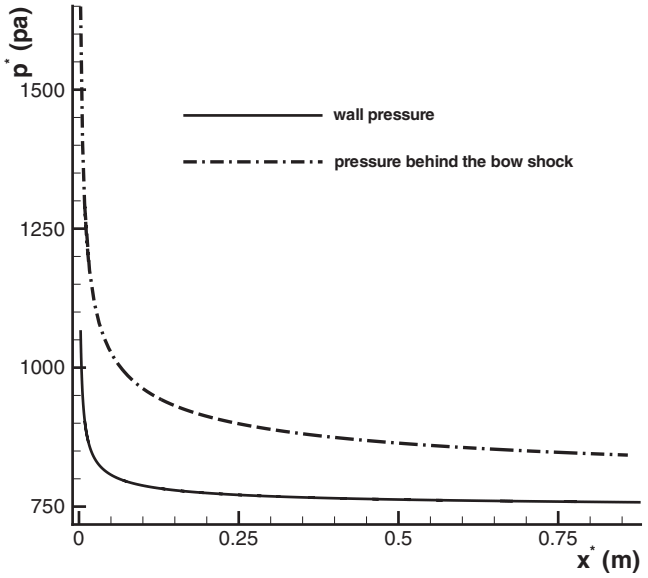

FIG. 6. Distributions of wall pressure and pressure behind the shock.

method is compared to the experimental measurements of Maslov *et al.* and self-similar boundary-layer solution. According to the experiments of Maslov *et al.*, viscous-inviscid interaction is strong within the region of 0.2 mm$<x^*<$33 mm ($50.99<R<654.98$). Figures 6 and 7 show that pressure and Mach number have large gradients upstream of the location of $x^*=33$ mm ($R=654.98$), which is consistent with the experimental results.

Figures 8 and 9 show distributions of dimensionless streamwise velocity u^*/u_∞^* and normalized Mach number M/M_∞ in wall-normal direction at three different locations of $x^*=96$, 121, and 138 mm ($R=1134.46, 1254.19, 1329.66$). Current numerical simulation results are compared to self-similar boundary-layer solution and experimental measurements of Maslov *et al.* In these two figures, η is defined as $\eta=y^*/L^*$. Solid lines represent M/M_∞ and u^*/u_∞^* obtained from self-similar solution. Unfilled symbols represent experimental measurements of Maslov *et al.* whereas the other three lines stand for current numerical simulation results. The good agreement between numerical simulation results indicate that the flat plate boundary layer has reached a self-similar state far downstream of the leading edge, which is evaluated in the paper of Maslov *et al.* by comparing experimental measurements. Figures 8 and 9 show that numerical simulation results agree well with experimental measurements and self-similar solution near the plate. However, in the region of $\eta>5$, numerical simulation results have a better agreement with experimental measurements. The difference between numerical simulation results and self-similar solution is mainly caused by viscous-inviscid interaction because the effect of bow shock is neglected in self-similar solution. The analysis of Figs. 8 and 9 indicate that steady base flow is accurately computed by the fifth-order shock-fitting method.

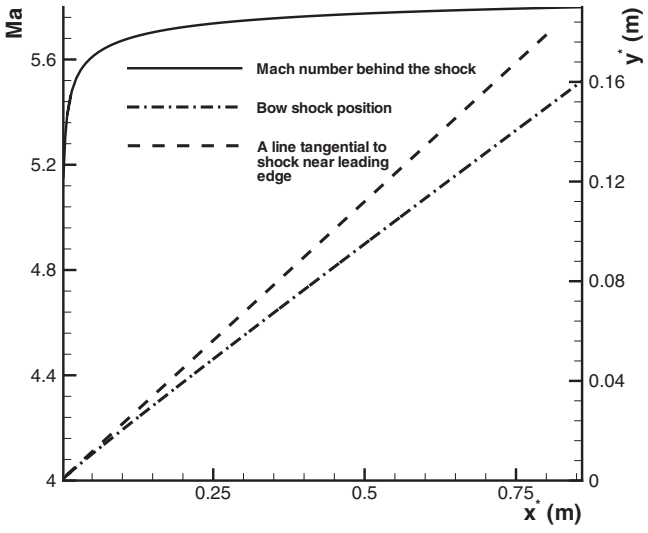

FIG. 7. Shock position and distribution of Mach number behind the shock.

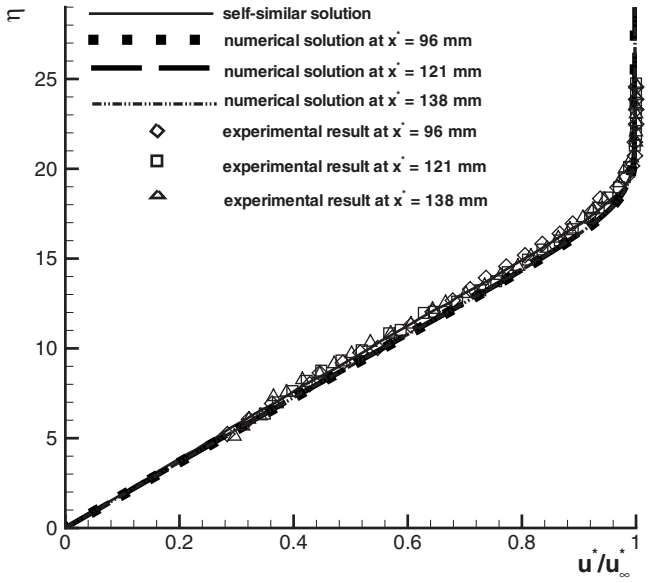

FIG. 8. Distributions of dimensionless streamwise velocity in wall-normal direction at three different locations.

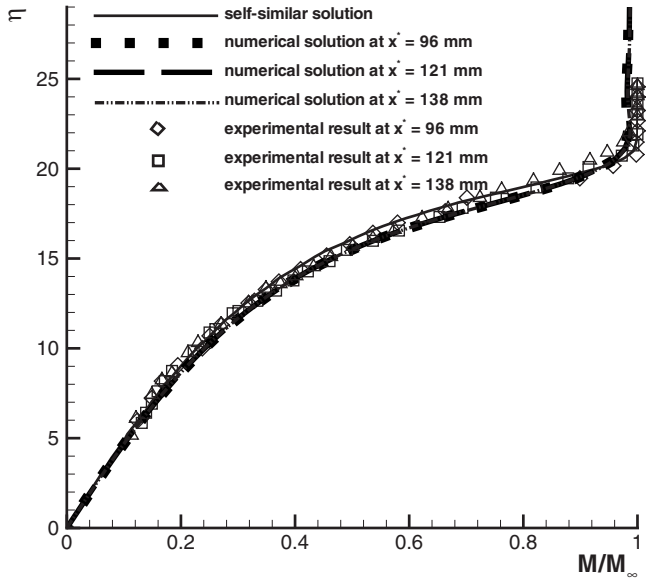

FIG. 9. Distributions of normalized Mach number in wall-normal direction at three different locations.

V. STABILITY CHARACTERISTICS OF BOUNDARY-LAYER WAVES

Stability characteristics of boundary-layer waves of the Mach 5.92 flow is studied by LST using a multidomain spectral method of Malik.[30] Velocity, pressure, and temperature disturbances are represented by harmonic waves of the form

$$\begin{Bmatrix} \tilde{u} \\ \tilde{v} \\ \tilde{w} \\ \tilde{p} \\ \tilde{T} \end{Bmatrix} = \begin{Bmatrix} \hat{u}(y) \\ \hat{v}(y) \\ \hat{w}(y) \\ \hat{p}(y) \\ \hat{T}(y) \end{Bmatrix} e^{i(\alpha x+\beta z-\omega t)}. \tag{21}$$

The two parameters, α and β, are wave number components in streamwise and spanwise directions, and ω is circular frequency. For two-dimensional wall perturbations, $\beta=0$. Substituting disturbances in Eq. (21) and steady base flow into linearized Navier–Stokes equations, an ordinary-differential-equation (ODE) system is obtained, i.e.,

$$\left(A\frac{d^2}{dy^2}+B\frac{d}{dy}+C\right)\phi=0, \tag{22}$$

where ϕ is disturbance vector defined by $\{\hat{u},\hat{v},\hat{p},\hat{T},\hat{w}\}^T$. The coefficient matrices of A, B, and C are given in Malik's paper.[30] In spatial stability analysis, the two parameters, ω and β, are specified as real numbers. The streamwise wave number, α, is a complex number and solved as the eigenvalue of the ODE system. The complex wave number α can be expressed as

$$\alpha=\alpha_r+i\alpha_i, \tag{23}$$

where $-\alpha_i$ is local growth rate. A boundary-layer wave is unstable when $\alpha_i<0$ whereas it is stable when $\alpha_i>0$. The points $\alpha_i=0$ are called neutral points of a boundary-layer wave. A wave is generally unstable only in certain domains bounded by neutral points. The real part, α_r, is local wave number which can be used to define local phase velocity,

$$a=\frac{\omega}{\alpha_r}. \tag{24}$$

Both wave number and phase velocity can be used to identify a boundary-layer wave.

Steady base flow needed for LST analysis can be obtained either by numerically solving Navier–Stokes equations or by computing a self-similar boundary-layer solution. Although numerical simulation result is more accurate than self-similar solution, it is inconvenient to use numerically simulated steady base flow for LST analysis at series of locations. Therefore, the self-similar boundary-layer solution is used in current LST study.

Figure 10(a) shows profiles of streamwise velocity and temperature in wall-normal direction at the location of $x^*=0.159$ m ($R=1437.71$). Numerical simulation results are compared to self-similar solutions in the figure. Profiles of first- and second-order derivatives of streamwise velocity and temperature are compared in Figs. 10(b) and 10(c), respectively. These three figures show that numerical simulation result agrees well with self-similar solution. The only exception is the small difference in the second-order derivatives near the edge of the boundary layer. The disagreement of numerical simulation results with self-similar solution in second-order derivatives is mainly caused by the effect of bow shock and nonparallel effect. Unlike self-similar solution, both effects are taken into account in numerical simulation. It was tested by Ma and Zhong[13] that linear stability characteristics based on self-similar solution were very close to those based on numerically simulated steady base flow.

Figure 11 shows eigenvalue spectra of boundary-layer waves at a frequency of $f^*=100$ kHz at $x^*=0.189$ m ($F=53.03\times10^{-6}$, $R=1567.48$). The figure shows wave spec-

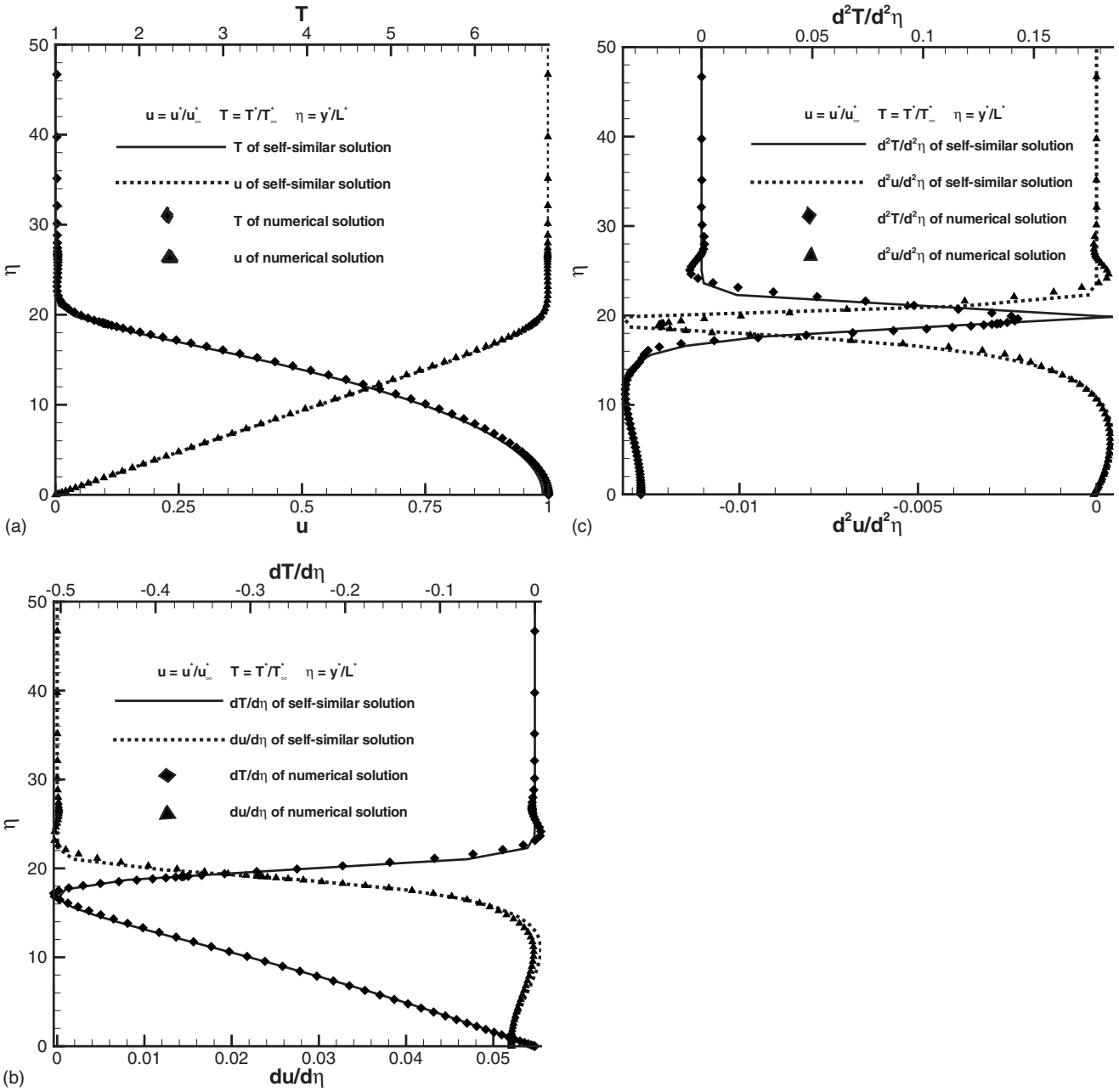

FIG. 10. Profiles of streamwise velocity and temperature and their derivatives in wall-normal direction at the location $x^*=0.159$ m ($R=1437.71$).

tra corresponding to fast acoustic wave, entropy and vorticity waves, and slow acoustic wave. The two discrete waves marked by circles are modes F and S. They are identified by corresponding eigenfunctions of u_r' and p_r', as shown in Figs. 12(a) and 12(b). The two figures show that eigenfunctions decrease quickly outside of the boundary layer, which indicates that these waves exist in the boundary layer. Mode F is a stable mode, which was called mode I by Ma and Zhong.[13,14] This mode originates from fast acoustic spectrum on the left side of the figure and passes entropy and vorticity spectra at the center as dimensionless frequency increases. Mode S originates from slow acoustic spectrum on the right side of the figure. It becomes unstable in certain range of dimensionless frequency. The figure also shows that mode S at the frequency of $f^*=100$ kHz is unstable at $x^*=0.189$ m ($R=1567.48$) with $\alpha_i<0$.

Figure 13 shows dimensionless phase velocities of boundary-layer waves at two locations of $x^*=0.159$ m and $x^*=0.189$ m ($R=1437.71$ and 1567.48) as a function of dimensionless circular frequency. The three horizontal dashed lines represent dimensionless phase velocities of fast acoustic wave ($a=1+M_\infty^{-1}$), entropy and vorticity waves ($a=1$), and slow acoustic wave ($a=1-M_\infty^{-1}$), respectively. The excellent agreement of phase velocities at two different locations indicates that phase velocity is approximately a function of dimensionless circular frequency only. The figure clearly shows that mode F originates from fast acoustic spec-

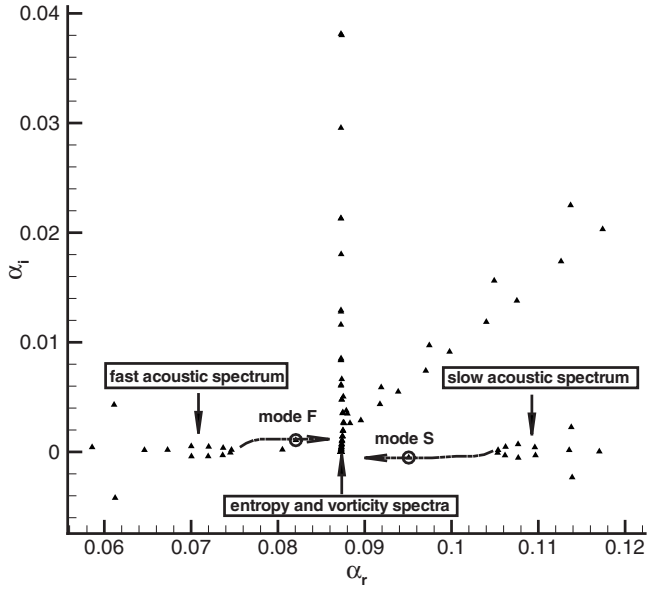

FIG. 11. Eigenvalue spectra of boundary-layer waves at the frequency of $f^*=100$ kHz at $x^*=0.189$ m ($R=1567.48$).

trum. As ω increases, phase velocity of mode F decreases. When mode F passes entropy and vorticity spectra near $\omega=0.1$, there exists a jump of phase velocity, which is consistent with theoretical analysis of Fedorov and Khokhlov.[31] On the other hand, mode S originates from slow acoustic spectrum. The figure also shows that mode S synchronizes with mode F at the point of $\omega_s=0.115\ 63$ and $a_s=0.930\ 76$.

At the synchronization point, dimensionless phase velocities of modes S and F are the same, and their eigenfunctions have similar profiles as shown in Fig. 14. In this figure, flow fluctuations, p_r' and u_r', in wall-normal direction are normalized by pressure fluctuation on the wall. The figure shows that flow fluctuations are confined within the boundary layer. Except the differences near edge of the boundary layer, eigenfunctions of modes F and S agree very well at the synchronization point. Although Fig. 13 shows that the synchronization point has a constant value of dimensionless circular frequency ($\omega_s=0.11563$), the dimensional location of the synchronization point, x_s^*, are different for different dimensionless frequencies F. The synchronization location in x^* coordinate for a given dimensionless frequency can be calculated using the following formula:

$$x_s^* = \frac{(\omega_s/F)^2}{\mathrm{Re}_\infty^*}. \tag{25}$$

This equation indicates that the synchronization point moves upstream with dimensionless frequency increasing.

Figure 15 shows growth rates of modes F and S at the same set of locations as a function of dimensionless circular frequency. The horizontal dotted line stands for neutral waves ($\alpha_i=0$). In Fig. 15, the growth rates of either mode S or mode F are approximately functions of dimensionless circular frequency only. Mode S is unstable in the region from $\omega_{\mathrm{I}}=0.008\ 27$ to $\omega_{\mathrm{II}}=0.184\ 65$, whereas mode F is always stable. For unstable mode S, it is also noticed that mode S around and downstream of the synchronization point is more

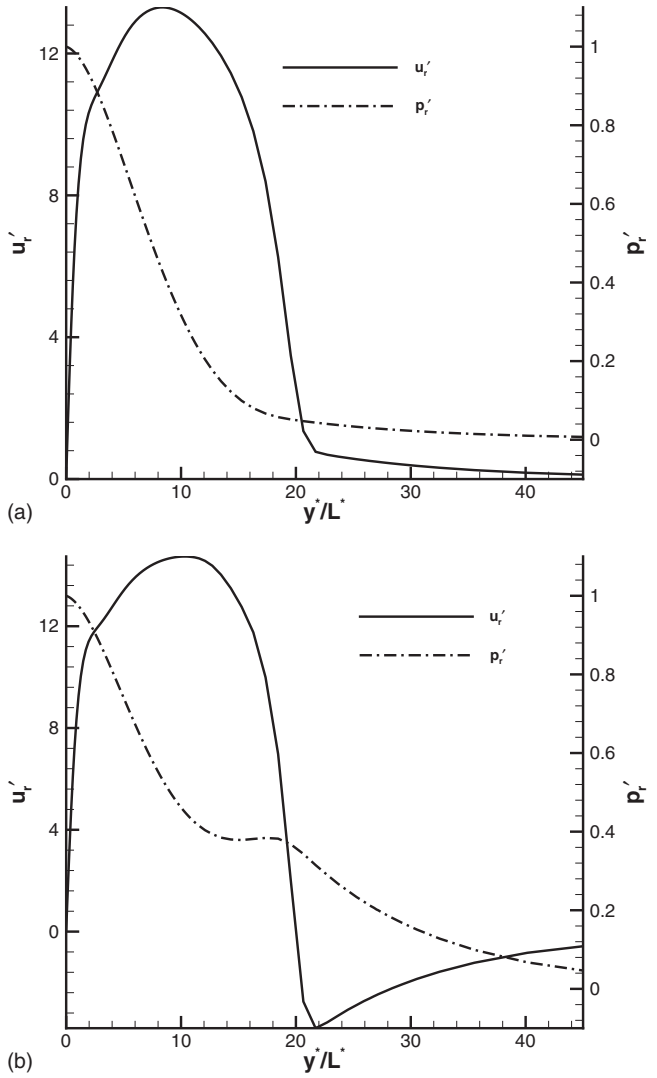

FIG. 12. Eigenfunctions of streamwise velocity and pressure of discrete boundary-layer waves: (a) mode F; (b) mode S.

unstable than that upstream of the synchronization point. The parameters ω_{I} and ω_{II} are called branches I and II neutral points of mode S. The figure shows that mode S is stable upstream of branch I neutral point and downstream of branch II neutral point. The locations of branches I and II neutral points in x^* coordinate, which changes with different dimensionless frequencies, can be calculated by

$$x_I^* = \frac{(\omega_{\mathrm{I}}/F)^2}{\mathrm{Re}_\infty^*}, \tag{26}$$

$$x_{\mathrm{II}}^* = \frac{(\omega_{\mathrm{II}}/F)^2}{\mathrm{Re}_\infty^*}. \tag{27}$$

Equations (26) and (27) indicate that when F increases, the corresponding coordinates of x_{I}^* and x_{II}^* decrease. In other words, branches I and II neutral points move upstream when F increases. Table I lists locations of synchronization point (x_s^*), branches I and II neutral points (x_{I}^*, and x_{II}^*), together with the coefficient b_n for the first nine sinusoidal components of periodic wall perturbation. The sinusoidal component at the frequency of $f_{10}^*=500$ kHz has a zero amplitude,

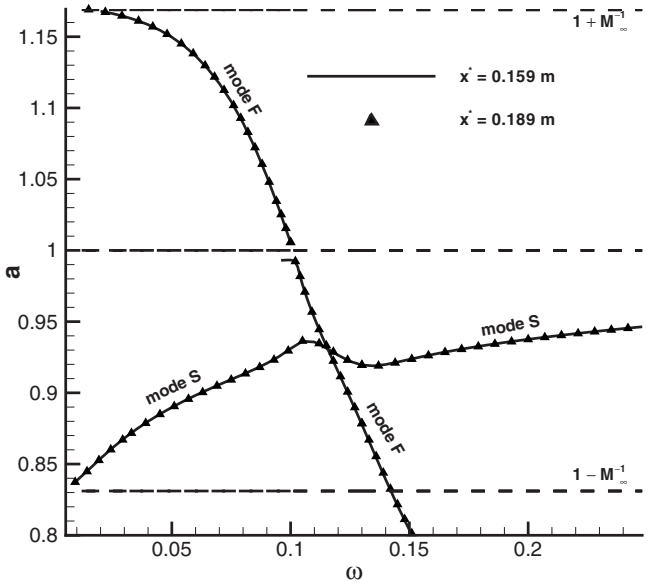

FIG. 13. Distributions of dimensionless phase velocities of boundary-layer waves at two different locations.

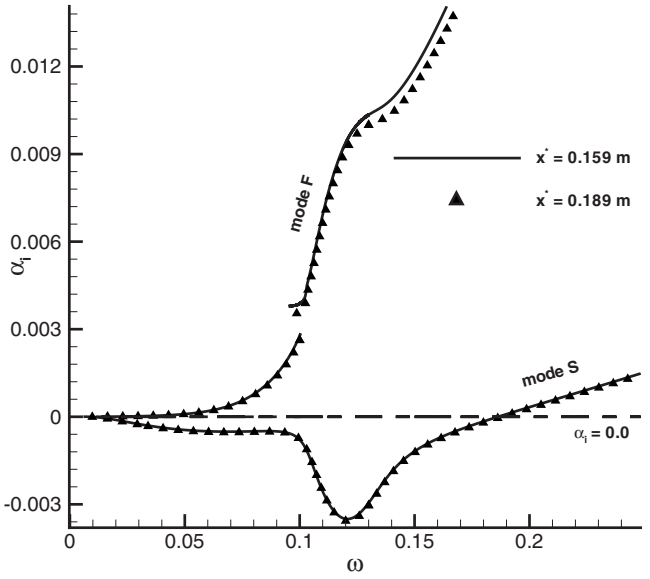

FIG. 15. Distributions of growth rates of modes *F* and *S* at two different locations.

as shown in Fig. 2. The other sinusoidal components are neglected because branch II neutral point moves upstream of the forcing region for sinusoidal component at a frequency higher than 500 kHz. As a result, the effect of mode *S* instability is weak when the frequency of sinusoidal component is higher than 500 kHz.

VI. RECEPTIVITY TO TWO-DIMENSIONAL WALL PERTURBATIONS

Receptivity of the hypersonic boundary layer to periodic two-dimensional wall perturbations is discussed in this section. The model of wall perturbation is proposed based on physical properties of the electric pulse generator used in the experiment of Maslov *et al.* Perturbations are introduced to steady base flow at a forcing slot with the leading and trailing edges at $x_i^*=33$ mm and $x_e^*=37$ mm ($R=654.98$ and 693.54). The specific slot width is selected based on the experiment of Maslov *et al.* The authors have investigated the effect of slot width on receptivity for some other cases. Those results are not discussed here because the focus of this paper is on the effect of wall perturbation on receptivity. Specifically, three types of wall perturbations are considered. The effect of wall perturbation on receptivity is investigated by three cases of numerical simulations. In each case, frequency of perturbation is equal to 50 kHz. The values of ϵ_1, ϵ_2, and ϵ_3 in Eq. (13) are assigned to be 1.0×10^{-7}, 1.0×10^{-5}, and 1.0×10^{-3}, respectively. Subsequent responses of the hypersonic boundary layer to wall perturbations are simulated by the fifth-order shock-fitting method. Details of three types of wall perturbations are listed in Table II.

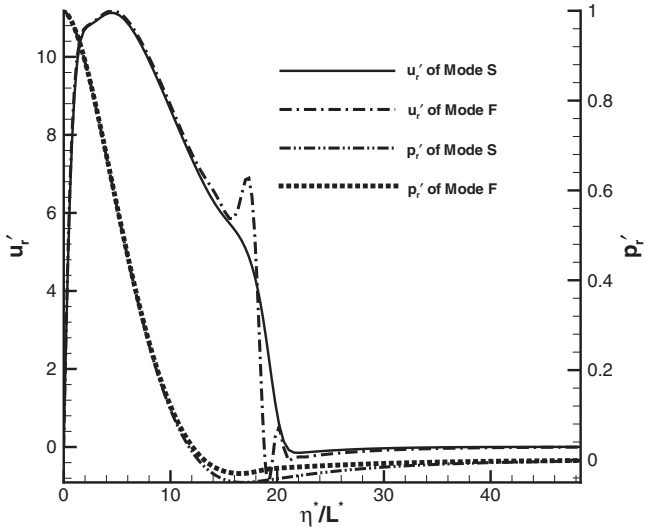

FIG. 14. Eigenfunctions of streamwise velocity and pressure of modes *F* and *S* at the synchronization point.

Table II shows that case A is the case of streamwise velocity perturbation, case B is the case of blowing suction, whereas case C is the case of temperature perturbation. Dimensional amplitudes of three types of wall perturbations are calculated according to Eq. (13). They are scaled by following free stream variables: $u_\infty^*=827.97$ m/s, $(\rho u)_\infty^*=44.01$ kg/m^2 s, and $T_\infty^*=48.69$ K, respectively. Although ϵ_1 is assigned to be 1.0×10^{-7}, dimensionless amplitude of streamwise velocity perturbation is equal to 1.073×10^{-4}. The difference comes from different scaling. In Eq. (13), ϵ_1 is scaled with the first order derivative of streamwise velocity, whereas dimensionless amplitude of streamwise velocity perturbation in Table II is scaled with streamwise velocity.

A. Receptivity to streamwise velocity perturbation

Receptivity of the Mach 5.92 flat plate boundary layer to streamwise velocity perturbation is studied first. The parameters of streamwise velocity perturbation are as follows: (A) streamwise velocity perturbation,

TABLE I. Locations of synchronization point (x_s^*), branches I and II neutral points (x_I^*, and x_{II}^*), and coefficients b_n for the first nine sinusoidal components of wall perturbation.

n	f^* (kHz)	$F_n \times 10^6$	x_s^* (m)	x_I^* (m)	x_{II}^* (m)	b_n
1	50	26.514 79	1.327 35	$6.789\ 77 \times 10^{-3}$	3.384 87	0.196 73
2	100	53.029 59	0.331 84	$1.697\ 44 \times 10^{-3}$	0.846 22	0.187 10
3	150	79.544 38	0.147 48	$7.544\ 18 \times 10^{-4}$	0.376 10	0.171 68
4	200	106.059 18	0.082 96	$4.24\ 360 \times 10^{-4}$	0.211 55	0.151 36
5	250	132.573 97	0.053 09	$2.715\ 91 \times 10^{-4}$	0.135 39	0.127 32
6	300	159.088 76	0.036 87	$1.886\ 04 \times 10^{-4}$	0.094 02	0.100 91
7	350	185.603 56	0.027 09	$1.385\ 67 \times 10^{-4}$	0.069 08	0.073 58
8	400	212.118 35	0.020 74	$1.060\ 90 \times 10^{-4}$	0.052 89	0.046 77
9	450	238.633 15	0.016 39	$8.382\ 43 \times 10^{-5}$	0.041 79	0.021 86

$$(Q_u, Q_v, Q_T) = (1,0,0), \quad \epsilon_1 = 1.0 \times 10^{-7}, \quad f^* = 50 \text{ kHz},$$

According to Eq. (13), case A introduces streamwise velocity perturbation to steady base flow, which models the ionization of gas molecules in the experiment of Maslov *et al.*

The profile function of streamwise velocity perturbation, $F(l_1)$, is written as

$$F(l_1) = -(20.25l_1^5 - 35.4375l_1^4 + 15.1875l_1^2)/2.456\ 88, \tag{28}$$

where the variable l_1 is defined in forcing region as

$$l_1 = 0.620\ 287 \begin{cases} 2(x^* - x_i^*)/(x_e^* - x_i^*), & \text{if } x^* \le 35 \text{ mm} \\ 2(x_e^* - x^*)/(x_e^* - x_i^*), & \text{if } x^* > 35 \text{ mm}. \end{cases} \tag{29}$$

Similar fifth-order-polynomial profile function has been used in receptivity studies of a Mach 8.0 flow over a sharp wedge to wall blowing suction.[12,25] Comparing with the generally used sinusoidal profile function, the specific fifth-order-polynomial profile function makes the perturbation at the edges (x_i^* and x_e^*) more smooth, being continuous up to the first-order derivative. In Eq. (28), the constant (2.456 88) is value of $F(l_1)$ at $l_1 = 0.620\ 287$, which is used to normalize profile function.

At first, two sets of grid structures are used to check grid independence of unsteady numerical simulation results. Figure 16 compares wall pressure fluctuation amplitude at a frequency of $f^* = 100$ kHz for two sets of grid structures. Amplitude distributions plotted in the figure are evaluated at the location of $x^* = 0.312$ m ($R = 2013.95$). It shows that amplitude distribution on 121×121 mesh agree well with that on 241×176 mesh. This figure indicates that the grid structure of 241×176 is good enough to ensure grid independence of unsteady numerical simulation results.

To show overall feature of the unsteady flow field, Fig. 17 shows contours of instantaneous pressure fluctuation induced by streamwise velocity perturbation at a frequency of $f^* = 50$ kHz. Downstream of the forcing region, excited pressure fluctuations are divided into two branches. One branch radiates into external flow outside the boundary layer and propagates along Mach lines (acoustic waves), while the other branch stays within the boundary layer (stable and unstable boundary-layer waves). Outside the boundary layer, forcing induced acoustic waves are interacted with Mach waves. Far downstream of the forcing region, stable wave decays owing to its inherent stability whereas unstable wave grows substantially due to its instability. Therefore, unstable wave becomes the dominant wave in the boundary layer. Similar characteristics of instantaneous pressure fluctuations are consistently shown in cases B and C. Figure 18 shows distribution of instantaneous wall pressure fluctuation in case

TABLE II. Dimensional and dimensionless amplitudes of three types of periodic wall perturbations.

Case	(Q_u, Q_v, Q_T)	Amplitude	Dimensionless amplitude
A	(1, 0, 0)	8.885×10^{-2} m/s	1.073×10^{-4}
B	(0, 1, 0)	4.401×10^{-4} kg/m^2 s	1.000×10^{-5}
C	(0, 0, 1)	4.869×10^{-2} K	1.000×10^{-3}

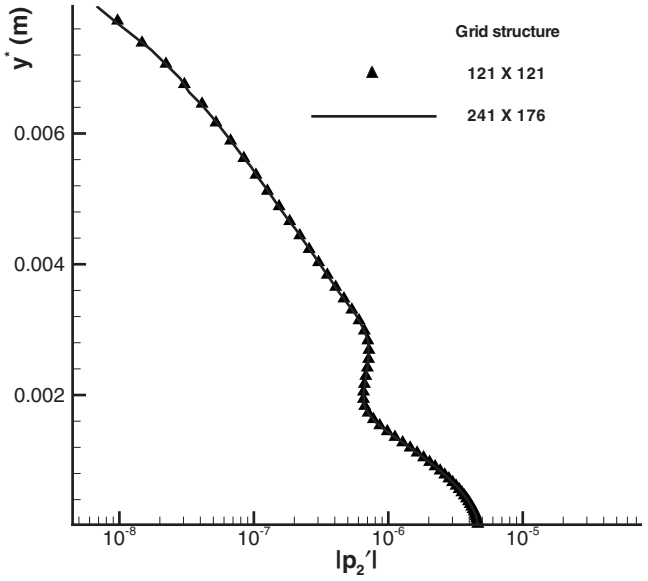

FIG. 16. Comparisons of wall pressure fluctuation amplitude for two sets of grid structures

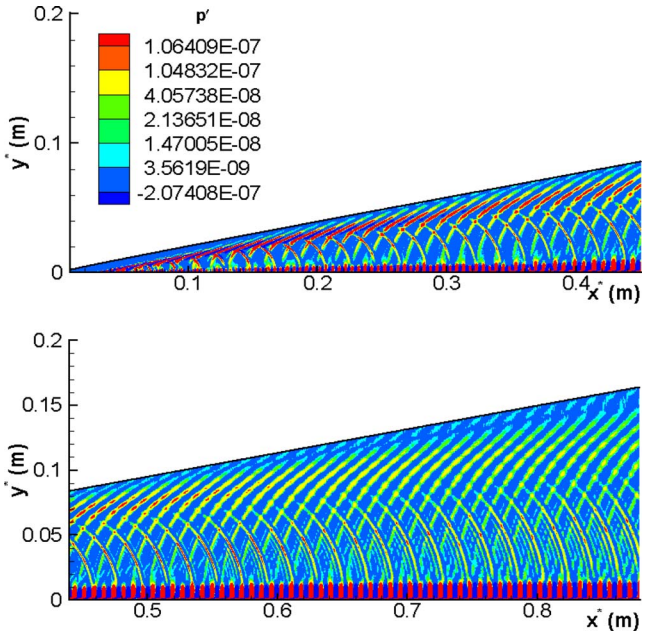

FIG. 17. (Color online) Contours of instantaneous pressure fluctuation induced by streamwise velocity perturbation at a frequency of $f^*=50$ kHz.

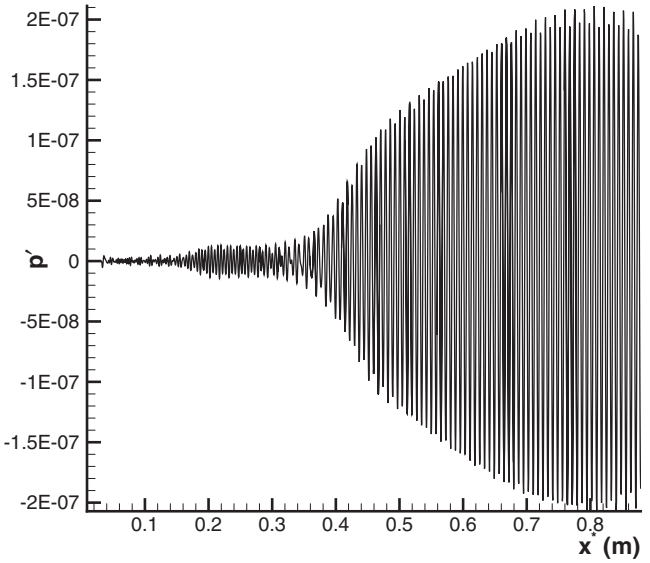

FIG. 18. Distribution of instantaneous wall pressure fluctuation in case A.

A. Amplification of pressure fluctuation from upstream to downstream indicates the excitation of unstable waves in the boundary layer. The standing wave structures indicate modulations between boundary-layer waves at different frequencies excited by sinusoidal components of periodic perturbation. It is also noticed in Fig. 18 that significant increase of pressure fluctuation starts around the location $x^*=0.35$ m ($R=2133.07$).

In order to identify and evaluate properties of unstable modes, a fast Fourier transform (FFT) is applied to instantaneous wall pressure fluctuation. In Fourier domain, the first nine sinusoidal components are considered. All the frequencies are expressed as

$$f_n^* = nf^* = 50n \ \text{kHz}, \tag{30}$$

where $n \in \{1,9\}$. In Eq. (30), f_1^* is the base frequency whereas the other eight frequencies f_n^* are n times of the base frequency. FFT of instantaneous wall pressure fluctuation leads to

$$p'(x^*,t^*) = \sum_{n=1}^{9} |p_n'(x^*)| e^{i[\phi_n'(x^*)-\omega_n^* t^*]}, \tag{31}$$

where $p'(x^*,t^*)$ represents instantaneous wall pressure fluctuation. In above equation, $|p_n'(x^*)|$ and $\phi_n'(x^*)$ are pressure fluctuation amplitude and phase angle excited by n^{th} sinusoidal component of streamwise velocity perturbation, respectively. Once $|p_n'(x^*)|$ and $\phi_n'(x^*)$ are computed, a local wave number (α_{rn}) and a local growth rate (α_{in}) at the frequency of f_n^* can be calculated by

$$\alpha_{rn} = L^* \frac{d\phi_n'}{dx^*}, \tag{32}$$

$$\alpha_{in} = -\frac{L^*}{|p_n'|}\frac{d|p_n'|}{dx^*}, \tag{33}$$

where L^* is the length scale of local boundary layer thickness as defined in Eq. (11). Values of α_{rn} and α_{in} will represent true wave number and growth rate only if pressure fluctuation is dominated by a single wave. Otherwise, pressure fluctuation needs to be further decomposed in order to check properties of a specific mode. For example, Tumin *et al.*[12] decomposed pressure fluctuation at a location just downstream of the blowing-suction slot with a biorthogonal eigenfunction system, where mode *F*, mode *S*, and acoustic modes coexisted and none of them was dominant.

In Eq. (33), wall pressure fluctuation is picked up to calculate growth rate. It needs to be pointed out that growth rate calculated from numerical simulation results depends on the choice of flow fluctuation. For example, growth rate bases on maximum perturbation in momentum flux will be different due to deformation of eigenfunctions.

Since our focus is on numerical simulation results, we only consider the later stage where unstable wave becomes the dominant wave in the boundary layer. In this case, Eqs. (32) and (33) can be used to check properties of unstable mode. Figure 19 shows amplitude distributions of wall pressure fluctuation induced by the first nine sinusoidal components of periodic wall oscillation. It is noticed that only perturbations at frequencies of f_n^* ($n<6$), as shown in Figs. 19(a) and 19(b) have apparent amplitude growths downstream of the forcing region. The fluctuation at the frequency of f_1^* grows very slowly, whereas the perturbations at other five frequencies start to decrease far before reaching the corresponding LST predicted branch II neutral points as listed in Table I. For fluctuation at even higher frequencies, there are no dramatic amplitude increases downstream of the forcing region.

Figure 20 compares growth rate computed by Eq. (33) and that obtained from LST of pressure fluctuation at the frequency of $f_2^*=100$ kHz. This figure shows that numeri-

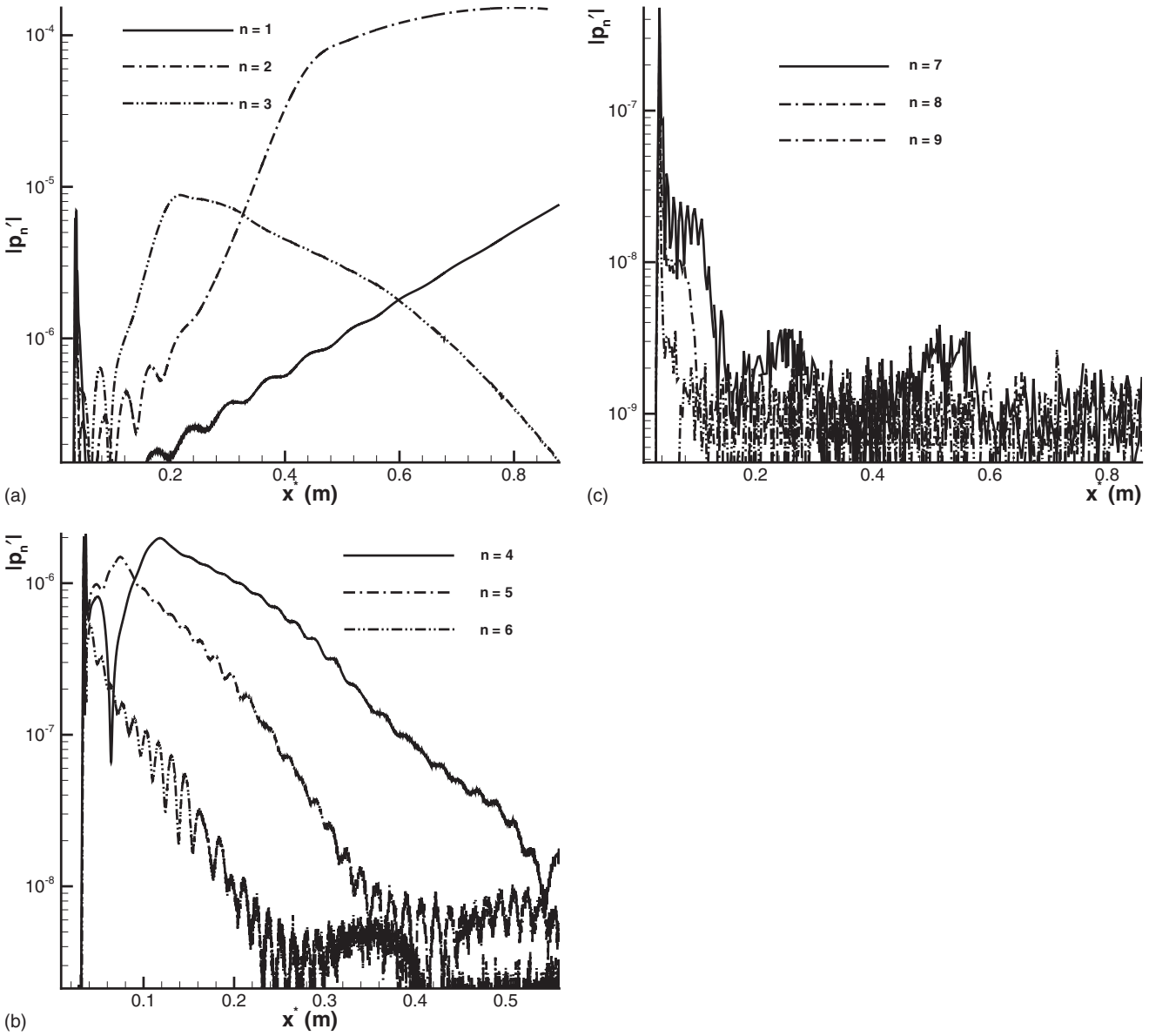

FIG. 19. Amplitude distributions of wall pressure fluctuation at different frequencies in case A ($f_n^*=nf_1^*$, $f_1^*=50$ kHz).

cally computed growth rate has a good agreement with LST predicted growth rate in a region from $\omega=0.11$ to $\omega=0.13$, which indicates that the unstable mode in the boundary layer is mode *S*. When dimensionless circular frequency is larger than 0.13, mode *S* obtained by numerical simulation becomes more stable than that predicted by LST. As a result, pressure fluctuation starts to decrease far before the LST predicted branch II neutral point, which is clearly shown in Fig. 19. For example, for the case of $n=3$, amplitude of pressure perturbation should keep increasing until $x^*=0.376\ 10$ m ($R=2211.18$), the corresponding branch II neutral point of mode *S* predicted by LST. However, pressure fluctuation in numerical simulation stops increasing at the location of $x^*=0.2$ m ($R=1612.45$), far upstream of LST predicted location. Such results are consistently noticed in all three cases of receptivity simulations considered in current study. Downstream of $\omega=0.13$, difference between growth rates obtained by LST and those computed from numerical simulation may be caused by nonparallel effect, the pressure gradient, and bow shock. These factors are neglected in current LST analysis.

Both our simulations and previous work of Ma and Zhong[5,13,14] consistently get similar results that higher frequency perturbations damp even if they should be amplified according to LST. According to Egorov *et al.*,[24] the stabilization of boundary layer wave might be caused by nonparallel effect because growth rate of Mack second mode obtained from nonparallel LST is significantly lower than that obtained from parallel LST. In current simulation, there are about 16 grid points per wavelength for the highest frequency disturbances.

Figure 21 compares wave numbers computed by Eq. (32) and that obtained from LST of pressure fluctuation at the frequency of $f_2^*=100$ kHz. The good agreement of the two sets of wave numbers in downstream region of $\omega>0.09$ also confirms that mode *S* is the unstable mode in

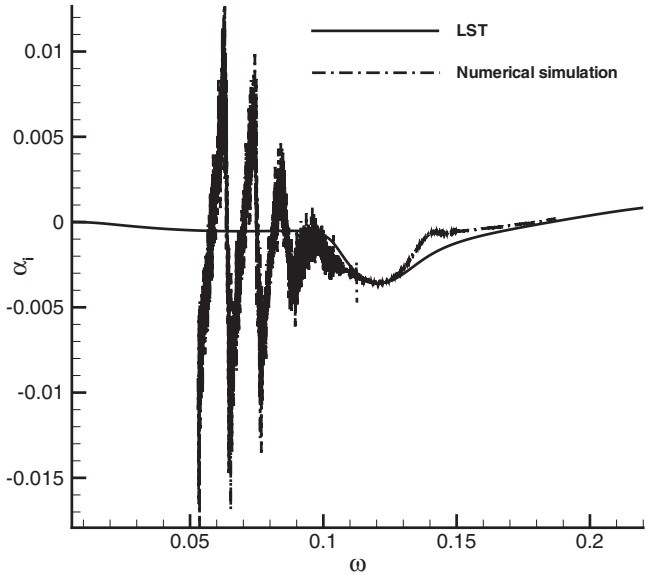

FIG. 20. Comparison of growth rate computed from numerical simulation and that obtained by LST of pressure fluctuation at the frequency of $f_2^*=100$ kHz.

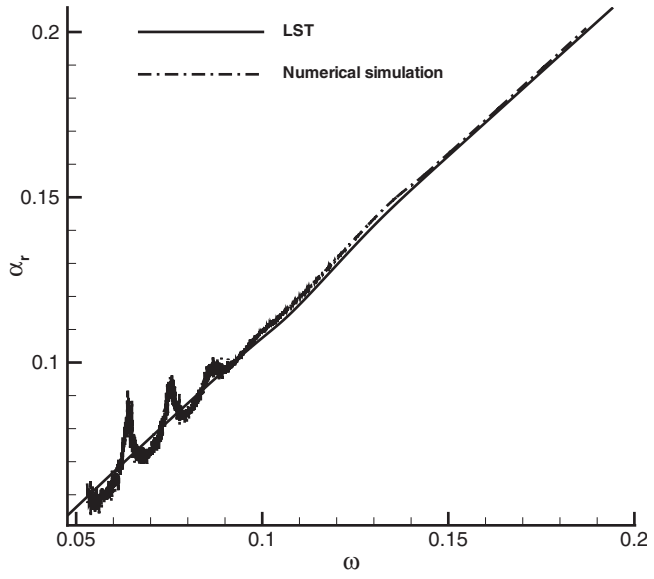

FIG. 21. Comparison of wave number computed from numerical simulation and that obtained by LST of pressure fluctuation at the frequency of $f_2^*=100$ kHz.

the boundary layer. The agreement is not as good in upstream region because mode *F*, mode *S*, and acoustic modes coexist in the boundary layer. In order to check the properties of mode *S*, pressure fluctuation in upstream region needs to be further decomposed into individual wave components.

As has been demonstrated in Fig. 15, mode *S* is more unstable around and downstream of the synchronization point. Therefore, in Fig. 19(a), pressure fluctuation at the frequency of $f_1^*=50$ kHz increases slowly downstream of the forcing region because mode *S* is only slightly unstable upstream of the corresponding synchronization point at $x_s^*=1.327\ 35$ m ($R=4153.98$). For pressure fluctuations at frequencies of f_n^* $(1<n<6)$, significant amplitude growths start at locations approximately the same as the corresponding synchronization points listed in Table I because mode *S* is more unstable around and downstream of the synchronization point. Pressure fluctuation at higher frequencies decrease downstream of the forcing region because forcing slot is located downstream of the corresponding synchronization points. It needs to be emphasized that forcing slot is still located within the unstable region of mode *S*, upstream of the corresponding LST predicted branch II neutral points. Such result is consistent with what we have found in receptivity study of a Mach 8 flow over a sharp wedge of a half angle of 5.3° to wall blowing suction.[25] It seems the synchronization point plays an important role in the excitation of mode *S* by wall perturbations, i.e., mode *S* is strongly excited only when forcing slot is located upstream of the synchronization point. When forcing slot is downstream of the synchronization point, there is very little excitation of mode *S*, despite the fact that forcing slot is still located within the unstable region of mode *S*. Further theoretical studies are needed to confirm and explain the role of the synchronization point in the excitation of mode *S*.

B. Effect of three perturbation types on receptivity

To investigate the effect of perturbation type on receptivity, two more cases of wall perturbations are considered. Numerical simulation results of these two cases are compared with those of case A. The parameters of these two cases of wall perturbations are as follows: (B) blowing suction,

$$(Q_u,Q_v,Q_T)=(0,1,0),\quad \epsilon_2=1.0\times10^{-5},\quad f^*=50\ \text{kHz},$$

(C) temperature perturbation,

$$(Q_u,Q_v,Q_T)=(0,0,1),\quad \epsilon_3=1.0\times10^{-3},\quad f^*=50\ \text{kHz}.$$

According to Eq. (13), case B introduces wall-normal mass flux to steady base flow, which models glow discharge in the experiment of Maslov *et al.* Temperature perturbation models streamwise extended oval on the plate observed in the experiment of Maslov *et al.* when voltages on electrodes were increased to 700 V.

The profile function of blowing suction, $G(l_2)$, is the same as what we have used in receptivity studies of a Mach 8 flow over a sharp wedge to wall blowing suction,[12,25] i.e.,

$$G(l_2)=\frac{1}{2.456\ 88}\begin{cases}20.25l_2^5-35.4375l_2^4+15.1875l_2^2, & \text{if } l_2\le 1\\ -20.25(2-l_2)^5+35.4375(2-l_2)^4-15.1875(2-l_2)^2, & \text{if } l_2>1,\end{cases} \tag{34}$$

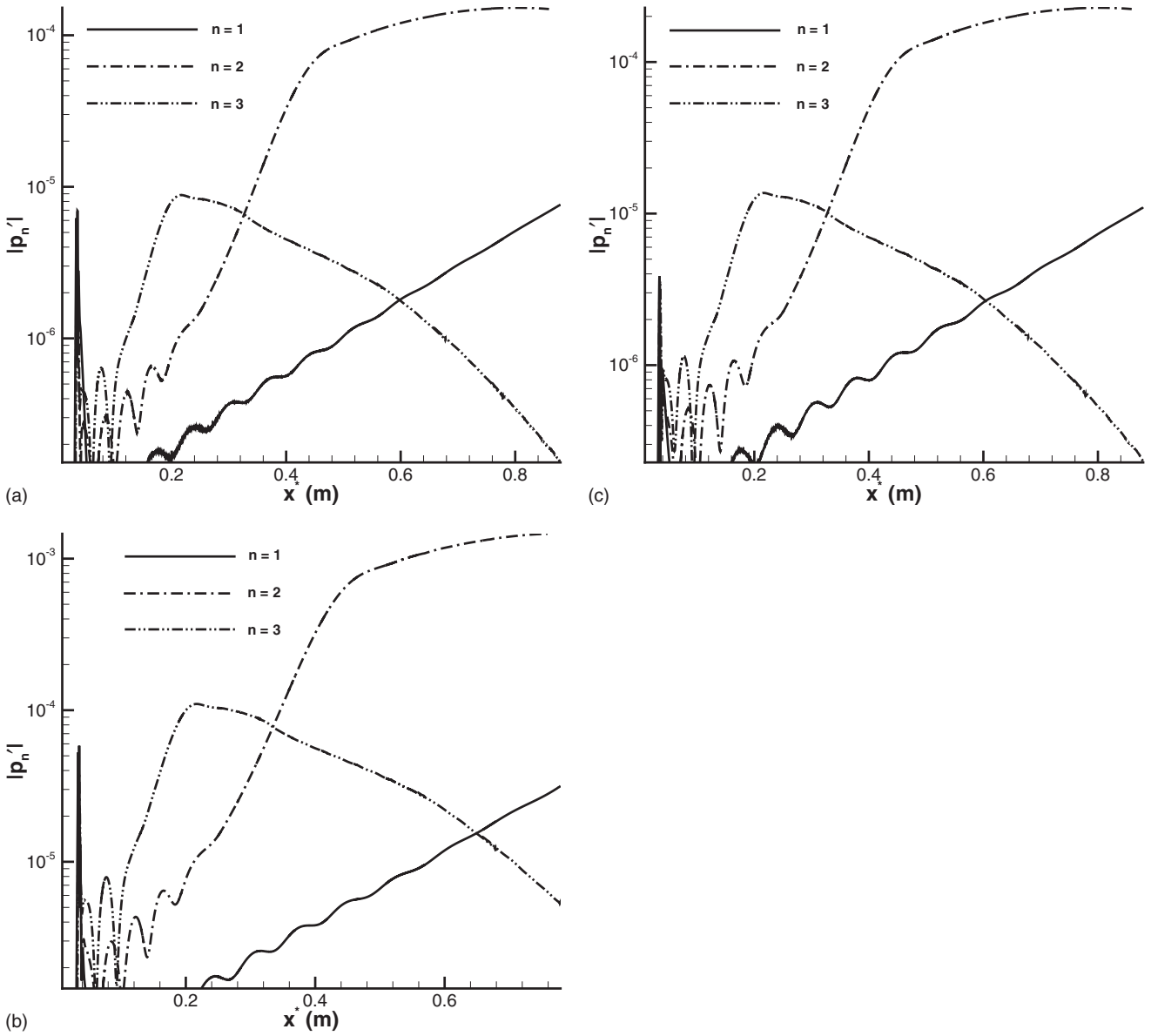

FIG. 22. Amplitude distributions of wall pressure fluctuations at the frequency of 50 kHz ($n=1$), 100 kHz ($n=2$), and 150 kHz ($n=3$) for three cases of wall perturbations: (a) case A; (b) case B; (c) case C.

with the variable l_2 being expressed as

$$l_2 = \frac{2(x^* - x_i^*)}{x_e^* - x_i^*}. \tag{35}$$

Again, the constant of 2.456 88 in Eq. (34) is value of the profile function at $l_2=0.620\ 287$, which is used to normalize $G(l_2)$.

The profile of temperature perturbation is the reverse of streamwise velocity perturbation given by Eq. (28), i.e., temperature perturbation is positive within the forcing region,

$$H_1(l_3) = (20.25l_3^5 - 35.4375l_3^4 + 15.1875l_3^2)/2.456\ 88. \tag{36}$$

The constant of 2.456 88 is value of $H_1(l_3)$ at $l_3=0.620\ 287$, which is used to normalize the profile function. The variable l_3 is defined exactly the same as l_1 in Eq. (29).

Figure 22 shows amplitude distributions of wall pressure fluctuations at three frequencies of 50, 100, and 150 kHz for three cases of wall perturbations. Amplitude distributions for pressure fluctuation at even higher frequency are neglected in this figure because the corresponding pressure fluctuation amplitudes are comparatively low. Specifically, Figs. 22(a)–22(c) show results of streamwise velocity perturbation, blowing suction, and temperature perturbation, respectively. It is clearly shown that pressure fluctuations at these three frequencies have similar properties. The pressure perturbation at the frequency of $f_1^*=50$ kHz increases slowly downstream of the forcing region because mode S is slightly unstable upstream of the corresponding synchronization point at $x_s^*=1.327\ 35$ m ($R=4153.98$). For fluctuations at frequencies of f_2^* and f_3^*, significant amplitude growths start at locations approximately the same as the corresponding synchronization points at $x_s^*=0.331\ 84$ m and $x_s^*=0.147\ 48$ m ($R=2077.00$ and 1384.64) because mode S

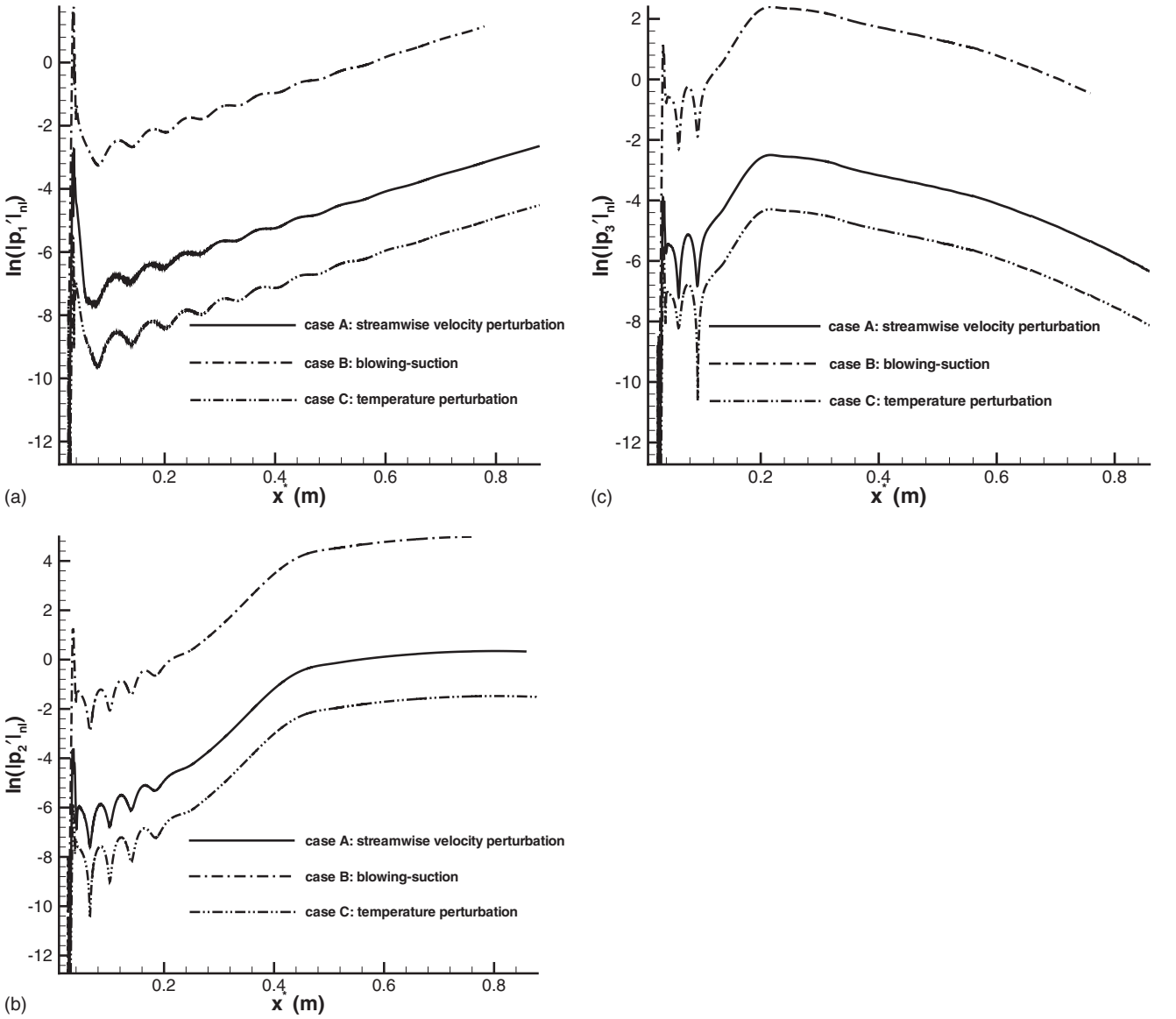

FIG. 23. Normalized amplitude comparison of wall pressure fluctuation at three frequencies for cases A, B, and C: (a) $f_1^*=50$ kHz; (b) $f_2^*=100$ kHz; (c) $f_3^*=150$ kHz.

is more unstable around and downstream of the synchronization point. Downstream of the forcing region, fluctuation at the frequency of $f_2^*=100$ kHz has the maximum amplitude. Such results indicate that different wall perturbations lead to the same boundary-layer instability, which is mode *S* as has been identified in Figs. 20 and 21. Receptivity mechanism of the hypersonic boundary layer to wall perturbations is independent of specific perturbation type.

It is also noticed in Fig. 22 that pressure fluctuation amplitudes of blowing suction (case B) are higher than those of temperature perturbation (case C). In turn, pressure fluctuation amplitudes of temperature perturbation (case C) are higher than those of streamwise velocity perturbation (case A). In other words, the hypersonic boundary-layer flow is most sensitive to blowing suction.

In order to quantitatively show the effect of wall perturbation on receptivity, Figs. 23(a)–23(c) compare normalized amplitudes of pressure fluctuations for cases A, B, and C at three frequencies of $f_1^*=50$ kHz, $f_2^*=100$ kHz, and $f_3^*=150$ kHz, respectively. In these figures, $|p_1'|_{nl}$, $|p_2'|_{nl}$, and $|p_3'|_{nl}$ are normalized pressure fluctuation amplitudes obtained by dividing fluctuation amplitudes with the corresponding dimensionless amplitudes listed in Table II. Again, similar properties of pressure fluctuation amplitudes indicate that receptivity mechanism of the hypersonic boundary layer to wall perturbation is independent of perturbation type. These figures consistently show that instability waves excited by blowing suction have higher amplitudes than those excited by streamwise velocity perturbation. Whereas instability waves excited by streamwise velocity perturbation have higher amplitudes than those excited by temperature perturbation. These results are qualitatively consistent with the theoretical and numerical analysis of Fedorov and Khokhlov.[11] The boundary layer is much more sensitive to blowing suction than to streamwise velocity perturbation and temperature perturbation.

VII. SUMMARY

In this paper, the receptivity of a Mach 5.92 flat plate boundary layer to periodic two-dimensional wall perturbations is studied by numerical simulations and LST. The objectives of the current research are to study the receptivity of the hypersonic boundary layer to wall perturbations, and to investigate the effect of different wall perturbation on receptivity. Free stream flow conditions of the hypersonic boundary layer are the same as the leading edge receptivity experiments of Maslov *et al.*[4] Steady base flow is simulated by solving two-dimensional compressible Navier–Stokes equations with a combination of a fifth-order shock-fitting finite difference method and a second-order TVD scheme. The accuracy of numerically simulated steady base flow is validated by comparisons with the experimental measurements of Maslov *et al.* and self-similar boundary-layer solution. In receptivity simulations, three types of periodic two-dimensional wall perturbations, streamwise velocity perturbation, blowing suction, and temperature perturbation, are considered. All wall perturbations are introduced to steady base flow at a forcing slot located on flat plate. A model of wall perturbation is proposed based on physical properties of the electric pulse generator used in the experiment of Maslov *et al.* Stability characteristics of boundary-layer waves are identified and evaluated by comparing the results of LST and numerical simulations. The effect of different wall perturbation on receptivity process are studied by considering three cases of numerical simulations.

The main conclusions of the current study are as follows.

- All three types of periodic two-dimensional wall perturbations eventually result in the same type of instability wave (mode *S*) in the boundary layer, which indicates that receptivity mechanism of the hypersonic boundary layer to wall perturbation is independent of specific perturbation type.
- Instability waves excited by blowing-suction have higher amplitudes than those excited by streamwise velocity perturbation. Whereas instability waves excited by streamwise velocity perturbation have higher amplitudes than those excited by temperature perturbation. Therefore, the hypersonic boundary-layer flow is most sensitive to blowing suction and least sensitive to temperature perturbation.

ACKNOWLEDGMENTS

This work was sponsored by the Air Force Office of Scientific Research, USAF, under Grant Nos. FA9550-04-1-0029 and FA9550-07-1-0414, monitored by Dr. J. D. Schmisseur. The views and conclusions contained herein are those of the authors and should not be interpreted as necessarily representing the official polices or endorsements, either expressed or implied, of the Air Force Office of Scientific Research or the U. S. Government.

[1] L. M. Mack, "Linear stability theory and the problem of supersonic boundary-layer transition," AIAA J. **13**, 278 (1975).
[2] J. M. Kendall, "Wind tunnel experiments relating to supersonic and hypersonic boundary-layer transition," AIAA J. **13**, 290 (1975).
[3] M. R. Malik, R. S. Lin, and R. Sengupta, "Computation of hypersonic boundary-layer response to external disturbances," AIAA Paper 1999-0411 (1999).
[4] A. A. Maslov, A. N. Shiplyuk, A. Sidorenko, and D. Arnal, "Leading-edge receptivity of a hypersonic boundary layer on a flat plate," J. Fluid Mech. **426**, 73 (2001).
[5] Y. Ma and X. Zhong, "Receptivity of a supersonic boundary layer over a flat plate. Part 3. Effects of different types of free-stream disturbances," J. Fluid Mech. **532**, 63 (2005).
[6] E. Reshotko, "Is Re_θ/Me a meaningful transition criterion?" AIAA J. **45**, 1441 (2007).
[7] M. V. Morkovin, E. Reshotko, and T. Herbert, "Transition in open flow systems-a reassessment," Bull. Am. Phys. Soc. **39**, 1882 (1994).
[8] W. S. Saric, H. L. Reed, and E. J. Kerschen, "Boundary-layer receptivity to freestream disturbances," Annu. Rev. Fluid Mech. **34**, 291 (2002).
[9] M. E. Goldstein and L. S. Hultgren, "Boundary-layer receptivity to long-wave free-stream disturbances," Annu. Rev. Fluid Mech. **21**, 137 (1989).
[10] W. S. Saric, "Görtler vortices," Annu. Rev. Fluid Mech. **26**, 379 (1994).
[11] A. V. Fedorov and A. P. Khokhlov, "Receptivity of hypersonic boundary layer to wall disturbances," Theor. Comput. Fluid Dyn. **15**, 231 (2002).
[12] A. Tumin, X. Wang, and X. Zhong, "Direct numerical simulation and the theory of receptivity in a hypersonic boundary layer," Phys. Fluids **19**, 014101 (2007).
[13] Y. Ma and X. Zhong, "Receptivity of a supersonic boundary layer over a flat plate. Part 1: Wave structures and interactions," J. Fluid Mech. **488**, 31 (2003).
[14] Y. Ma and X. Zhong, "Receptivity of a supersonic boundary layer over a flat plate. Part 2: Receptivity to freestream sound," J. Fluid Mech. **488**, 79 (2003).
[15] A. V. Fedorov, "Excitation of Tollmien-Schlichting waves in a boundary layer by a periodic external source located on the body surface," Fluid Dyn. **19**, 888 (1984).
[16] A. Hanifi, P. J. Schmid, and D. S. Henningson, "Transient growth in compressible boundary layer flow," Phys. Fluids **8**, 826 (1996).
[17] E. Forgoston and A. Tumin, "Three-dimensional wave packet in a hypersonic boundary layer," Phys. Fluids **18**, 104103 (2006).
[18] A. Tumin, "Three-dimensional spatial normal modes in compressible boundary layers," J. Fluid Mech. **586**, 295 (2007).
[19] A. D. Kosinov and A. A. Maslov, "Growth of artificially induced disturbances in a supersonic boundary layer," Fluid Dyn. **19**, 703 (1985).
[20] A. A. Maslov and N. V. Semenov, "Excitation of natural oscillations in a boundary layer by an external acoustic field," Fluid Dyn. **21**, 400 (1986).
[21] A. D. Kosinov, A. A. Maslov, and N. V. Semionov, "An experimental study of generation of unstable disturbances on the leading-edge of a plate at M=2," J. Appl. Mech. Tech. Phys. **38**, 45 (1997).
[22] S. S. Collis and S. K. Lele, "Receptivity to surface roughness near a swept leading edge," J. Fluid Mech. **380**, 141 (1999).
[23] X. Zhong, "Leading-edge receptivity to free stream disturbance wave for hypersonic flow over a parabola," J. Fluid Mech. **441**, 315 (2001).
[24] I. V. Egorov, A. V. Fedorov, and V. G. Soudakov, "Direct numerical simulation of disturbances generated by periodic suction-blowing in a hypersonic boundary layer," Theor. Comput. Fluid Dyn. **20**, 41 (2006).
[25] X. Wang, "Numerical simulations of supersonic boundary-layer stability and receptivity," Ph.D. thesis, University of California at Los Angeles (2007).
[26] I. V. Egorov, V. G. Sudakov, and A. V. Fedorov, "Numerical modeling of the stabilization of a supersonic flat-plate boundary layer by a porous coating," Fluid Dyn. **41**, 356 (2006).
[27] X. Zhong and Y. Ma, "Boundary-layer receptivity of Mach 7.99 flow over a blunt cone to free-stream acoustic waves," J. Fluid Mech. **556**, 55 (2006).
[28] X. Zhong, "High-order finite-difference schemes for numerical simulation of hypersonic boundary-layer transition," J. Comput. Phys. **144**, 662 (1998).
[29] X. Zhong and T. Lee, "Nonequilibrium real-gas effects on disturbance/bow shock interaction in hypersonic flow past a cylinder," AIAA Paper No. 1996-1856 (1996).
[30] M. R. Malik, "Numerical methods for hypersonic boundary layer stability," J. Comput. Phys. **86**, 376 (1990).
[31] A. V. Fedorov and A. P. Khokhlov, "Prehistory of instability in a hypersonic boundary layer," Theor. Comput. Fluid Dyn. **14**, 359 (2001).